

Effects of a nozzle on the propeller wake in an oblique flow using modal analysis

Tianyuan Wang¹, Hongda Shi^{1,2,3,4}, Ming Zhao⁵ and Qin Zhang^{1,†}

¹College of Engineering, Ocean University of China, 238 Songling Road, Qingdao 266100, PR China

²Shandong Provincial Key Laboratory of Ocean Engineering, 238 Songling Road, Qingdao 266100, PR China

³Pilot National Laboratory for Marine Science and Technology (Qingdao), 1, Wenhai Road, Aoshanwei, Jimo, Qingdao 266237, PR China

⁴Qingdao Municipal Key Laboratory of Ocean Renewable Energy, Ocean University of China, Qingdao 266100, PR China

⁵School of Computing, Engineering and Mathematics, Western Sydney University, Penrith, NSW 2751, Australia

(Received 4 October 2022; revised 28 December 2022; accepted 28 January 2023)

The effect of a nozzle on the wake dynamics of a four-bladed propeller operating in an oblique flow is investigated via modal decomposition and flow visualization of the results obtained from numerical simulations using delayed detached eddy simulations. The wake characteristics and destabilization mechanisms of a non-ducted propeller (NP) and ducted propeller (DP) in axisymmetric and oblique flow conditions are systematically analysed. The wake characteristics on the windward side are very different from those on the leeward side in an oblique flow, and the nozzle has a crucial role in mitigating the asymmetry and weakening the wake deflection. More destabilization mechanisms are present in an oblique flow than in an axisymmetric flow, including the asymmetric evolution and destabilization of the helices on the windward and leeward sides of the NP wake, the interaction between the vortex shedding and the helices in the DP leeward region, and the generation of a tube-shaped wake envelope around the nozzle and its rolling-up. Moreover, the effect of the nozzle on wake meandering is discussed based on modal analysis.

Key words: vortex instability, vortex interactions, turbulence simulation

1. Introduction

Rotor devices (e.g. propellers, wind and tidal turbines) that are initially designed to operate under uniform and axisymmetric flow are sometimes required to work in off-design

† Email address for correspondence: zhangqin2000@ouc.edu.cn

conditions for manoeuvring (Felli & Falchi 2018; Huang, Qin & Pan 2022) or optimal energy extraction (Li & Yang 2021; Borg *et al.* 2022). For instance, when a ship changes its direction, the lateral flow can strongly modify the propeller propulsive loads, thus affecting the ship dynamic response and inducing the thruster–hull interaction (Viviani *et al.* 2007; Dubbioso, Muscari & Di Mascio 2013, 2014; Di Mascio, Muscari & Dubbioso 2014; Zhang, Ma & Liu 2018; Qiu *et al.* 2020). Analogously, in a large wind farm, to avoid the unfavourable wake interaction between two wind turbines, an active yaw control strategy has been adopted to deflect the upstream turbine wakes away from the downwind turbines and to increase the total power production of the wind turbine array (Bastankhah & Porté-Agel 2016; Zong & Porté-Agel 2020; Bossuyt *et al.* 2021; Li & Yang 2021). In this context, a deeper understanding of rotor wake dynamics and evolution mechanisms in an oblique flow is vital for optimizing rotor design and formulating control strategies.

Rotor wake vortex systems have been analysed for more than a century (Joukowsky 1912; Widnall 1972; Okulov & Sørensen 2007; Felli, Camussi & Di Felice 2011; Di Mascio *et al.* 2014). Conceptually, a rotor with N blades operating in a steady, axisymmetric flow consists of N tip vortices, N trailing edge vortices and N root vortices (or a hub vortex) (Okulov & Sørensen 2007; Micallef & Sant 2016). Each trailing edge vortex is generated by the spanwise gradient of the blade circulation $\partial\Gamma/\partial r$ and is shed from the blade edge in a direction normal to the blade trailing edge. At the tip and root sections of each blade, the trailing edge vortex further rolls up into two counterrotating vortices, i.e. tip and root vortices, each with strength Γ (Felli & Falchi 2018). Additionally, N root vortices coil around each other to form a hub vortex with strength $-N\Gamma$ (Okulov 2004; Zhang, Markfort & Porté-Agel 2012; Ashton *et al.* 2016). When the rotor operates in a non-uniform or oblique flow, apart from the vortex structures mentioned above, the vortex systems also involve shed vortices, which are generated by the time-dependent blade circulation $\partial\Gamma/\partial t$ and are shed in a direction parallel to the blade trailing edges (Di Mascio *et al.* 2014; Micallef & Sant 2016; Felli & Falchi 2018).

Tip vortices have attracted considerable attention due to their contribution to wake destabilization. The morphology of tip vortices and their instability are highly dependent on the blade geometry (e.g. blade number, blade skew and rake angles, as documented by Felli *et al.* 2011; Kumar & Mahesh 2017) and operative conditions (e.g. advance coefficient and inflow angle, see Di Mascio *et al.* 2014; Felli & Falchi 2018; Magionesi *et al.* 2018). Specifically, when a ring nozzle with a streamlined cross-section is fixed around a propeller, the tip vortices leaking from the gap between the blade tip and the nozzle inner sidewall undergo intense shear and vorticity redistribution (Wu, Ma & Zhou 2006), forming tip leakage vortices (Zhang & Jaiman 2019; Gong, Ding & Wang 2021; Shi *et al.* 2022). The tip vortices of the non-ducted propeller (NP) and the tip leakage vortices of the ducted propeller (DP) are referred to as helices in this paper for brevity.

Under yawed conditions, asymmetric evolution, instability and breakdown of helices were observed on the windward and leeward sides of the NP and DP (Dubbioso *et al.* 2013, 2014; Di Mascio *et al.* 2014; Felli & Falchi 2018; Huang *et al.* 2022; Li *et al.* 2022). For an NP operating in an oblique flow, a significant difference compared with the NP in an axisymmetric flow is the generation of the time-dependent shed vortices that induce the secondary vortex systems at the slipstream boundary via shear (Di Mascio *et al.* 2014; Felli & Falchi 2018). Moreover, the bending characteristics of the NP wake result in asynchronous helix ‘pairing’ on the leeward and windward sides (Felli & Falchi 2018). For yawed DPs, vortex shedding is generated at the leeward nozzle leading edge due to the yaw

misalignment, and the interaction between the vortex shedding and the helices accelerates wake destabilization in the leeward region (Huang *et al.* 2022; Li *et al.* 2022).

In large wind farms, an underlying mechanism that reduces power outputs and increases the fatigue loads of downwind turbines is far-wake meandering characterized by low-frequency and high-turbulence intensity (Viola *et al.* 2015; Bastankhah & Porté-Agel 2017; Foti *et al.* 2018a; Foti, Yang & Sotiropoulos 2018b; Mao & Sørensen 2018; Yang & Sotiropoulos 2019; Li & Yang 2021). The misalignment of upstream wind turbine wakes with downstream turbines has attracted considerable attention as this strategy can effectively reduce the power losses caused by wake meandering (Bastankhah & Porté-Agel 2016; Micallef & Sant 2016; Foti *et al.* 2019; Zong & Porté-Agel 2020; Bossuyt *et al.* 2021; Li & Yang 2021). Some literature has documented that wake meandering is related to the long-wave instability of the hub vortex (Felli *et al.* 2011; Iungo *et al.* 2013; Viola *et al.* 2014; Howard *et al.* 2015; Ashton *et al.* 2016; Foti *et al.* 2018b; Magionesi *et al.* 2018). However, a recent review by Yang & Sotiropoulos (2019) concluded that hub vortex instability does not cause wake meandering but may energize large-scale motion, which is consistent with the findings of Kang, Yang & Sotiropoulos (2014). Furthermore, a numerical investigation conducted by Foti *et al.* (2018a) reported that neither a nacelle model nor an unstable hub vortex is required for the existence of wake meandering. Mao & Sørensen (2018) modelled wake meandering without considering a hub vortex and noted that meandering is dominated by large-scale, low-frequency helical vortices experiencing a shear interaction with the free stream.

To explore the wake dynamic and destabilization mechanisms of a marine propeller, both experimental techniques, e.g. laser Doppler velocimetry (LDV) (Felli & Di Felice 2005; Felli *et al.* 2011) and particle image velocimetry (PIV) (Di Felice *et al.* 2004; Felli, Di Felice & Guj 2006; Felli & Falchi 2018), and high-accuracy numerical models, such as large eddy simulation (LES) (Verma, Jang & Mahesh 2012; Kumar & Mahesh 2017; Posa *et al.* 2019; Posa, Broglia & Balaras 2020, 2022; Posa & Broglia 2021; Wang *et al.* 2021b; Wang, Liu & Wu 2022), detached eddy simulation (DES) (Muscari, Di Mascio & Verzicco 2013; Di Mascio *et al.* 2014; Muscari, Dubbioso & Di Mascio 2017; Wang *et al.* 2019; Gong *et al.* 2021; Zhang *et al.* 2021) and its variants, including detached DES (DDES) (Zhang & Jaiman 2019; Shi *et al.* 2022) and improved DDES (IDDES) (Qin *et al.* 2021; Wang *et al.* 2021a; Huang *et al.* 2022; Li *et al.* 2022), have been employed.

Furthermore, some postprocessing tools based on experimental and numerical results have been used to explore the evolution mechanisms of propeller wakes. For example, time-resolved velocity signals monitored by experimental LDV (Felli *et al.* 2011) or numerical probes (Shi *et al.* 2022) are combined with time-frequency transform (or analysis) methods to explore the characteristic frequencies of flow phenomena and to investigate the energy transfer process in the propeller wake. The spectral analysis of individual spatial points can only qualitatively associate the flow signals with visible flow phenomena (Felli *et al.* 2011; Gong *et al.* 2021; Wang *et al.* 2021a; Shi *et al.* 2022) but cannot visualize the flow phenomena with specific frequencies. An alternative way to address this problem is to decompose the whole flow field and visualize the spatial modes using machine learning-based, reduced-order models (ROMs, Rowley & Dawson 2017; Taira *et al.* 2017; Brunton *et al.* 2022). Among various ROMs, proper orthogonal decomposition (POD, Lumley 1970; Sirovich 1987) and dynamic mode decomposition (DMD, Rowley *et al.* 2009; Schmid 2010) are commonly applied data-driven methods.

The POD and/or DMD have been widely used in analysing rotor wake experimental PIV (Paik *et al.* 2010; Nemes *et al.* 2014; Felli, Falchi & Dubbioso 2015; Kumar &

Mahesh 2015; Bastankhah & Porté-Agel 2017) and numerical results (Sarmast *et al.* 2014; Iungo *et al.* 2015; Debnath *et al.* 2017; Foti *et al.* 2018a; Magionesi *et al.* 2018; Qatramez & Foti 2021; Sun *et al.* 2021; De Cillis *et al.* 2022a,b; Shi *et al.* 2022; Wang *et al.* 2022). For a four-bladed propeller (blade frequency is four times the shaft frequency), Magionesi *et al.* (2018), Shi *et al.* (2022) and Wang *et al.* (2022) identified that the passage of helices and the pairing of adjacent helices are characterized by blade frequency and half blade frequency, respectively. Moreover, low-frequency signals lower than or equal to the shaft frequency are associated with wake meandering (Magionesi *et al.* 2018), as further confirmed by Shi *et al.* (2022), Foti *et al.* (2018a) and Bastankhah & Porté-Agel (2017) using reduced-order reconstruction. The modal analysis also enables the identification of other underlying destabilization mechanisms that are not easily detected in the spatiotemporally coupled flow field. For instance, based on the vorticity magnitude in the NP and DP wakes obtained by the DDES model, Shi *et al.* (2022) found that the helices interact with trailing edge vortices at the blade frequency and its multiples, where the blade frequency mode dominates this interaction mechanism. Furthermore, during the vortex interaction at the blade frequency, helices undergo short-wave instability, and numerous secondary vortices are formed between adjacent helices. Sarmast *et al.* (2014) locally analysed the velocity in the wind turbine wake achieved by LES and focused on the onset mechanism of helix instability. The authors discovered that an out-of-phase displacement of successive helices characterizes the most unstable modes, and these modes cause the pairing of adjacent helices, which is consistent with the findings of Sun *et al.* (2021).

Modal decomposition techniques have been widely employed in analysing the rotor wake in axisymmetric configurations. However, minimal attention has been given to the feasibility of the methods in oblique inflow conditions where several distinct but neighbouring spectral peaks may coexist in one successive helix as it travels downstream (Di Mascio *et al.* 2014). Another subject worth investigating is the effect of a nozzle on the propeller wake deflection and helix vorticity intensity in an oblique flow. The majority of studies compared only the wake dynamics of a single NP or DP operating at slight inflow angles ($\leq 30^\circ$) (Dubbioso *et al.* 2013; Di Mascio *et al.* 2014; Felli & Falchi 2018; Huang *et al.* 2022; Li *et al.* 2022), but a comprehensive comparison of the wake characteristics of a propeller with and without a nozzle over a wide range of inflow angles is rare. In the present work, numerical research on the wake dynamics of an NP and DP with the same propeller geometry working at five inflow angles ($\alpha = 0^\circ, 15^\circ, 30^\circ, 45^\circ$ and 60°) is conducted to evaluate the effect of the nozzle on the wake deflection and to explore the differences in the evolution characteristics and destabilization mechanisms between NP wakes and DP wakes in an oblique flow. The propeller (S5810 R) and nozzle (1393 type 19A) geometries are chosen, as the DP is designed to eliminate the undesirable hub vortex (Cozijn, Hallmann & Koop 2010; Cozijn & Hallmann 2012; Maciel, Koop & Vaz 2013; Koop *et al.* 2017) and it gives us a chance to evaluate the far-wake meandering in yawed conditions without interference from a hub vortex. A moderate advance coefficient of $J = 0.4$ is chosen because this operating condition is full of rich destabilization mechanisms (Magionesi *et al.* 2018; Zhang & Jaiman 2019; Shi *et al.* 2022).

In this paper, qualitative analysis of the wake destabilization, quantitative evaluation of the flow physics and spectrum-based modal identification methods are combined to gain a deeper insight into the rotor wake dynamics during realistic operational conditions. Figure 1 clarifies the structure of the paper and the links between two sections. The numerical setup is described in § 2. Comprehensive comparisons of destabilization

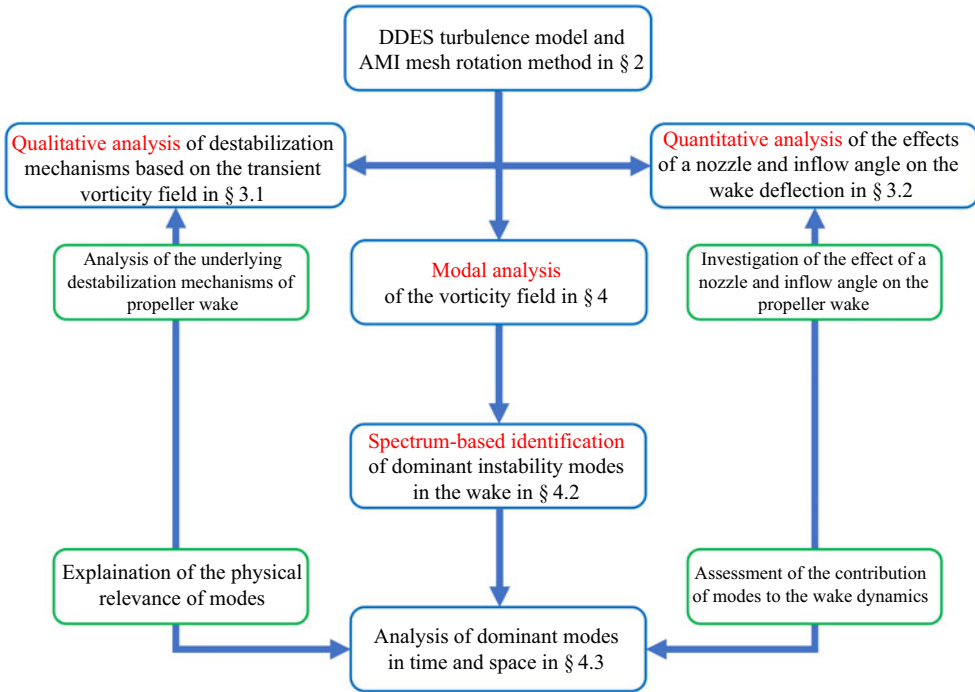


Figure 1. Framework structure of the paper.

mechanisms and wake deflection between NP wakes and DP wakes at different inflow angles are presented in § 3. Modal analysis of the wake vorticity based on POD and DMD is documented in § 4. The key conclusions are summarized in § 5.

2. Numerical method

The DDES model developed by Spalart *et al.* (2006) is employed to simulate transient flow. The turbulence model is described in this section and grid sensitivity studies are presented separately in § A.1.

2.1. Governing equations

The wakes of the NP and DP are simulated by solving the three-dimensional (3-D) incompressible Navier-Stokes equations. For an incompressible, single-phase Newtonian flow, the filtered mass and momentum equations are given by

$$\frac{\partial \bar{u}_i}{\partial x_i} = 0, \quad (2.1)$$

$$\frac{\partial \bar{u}_i}{\partial t} + \frac{\partial \bar{u}_i \bar{u}_j}{\partial x_j} = -\frac{1}{\rho} \frac{\partial \bar{p}}{\partial x_i} + \nu \frac{\partial^2 \bar{u}_i}{\partial x_i \partial x_j} - \frac{\partial D_{ij}}{\partial x_j}, \quad (2.2)$$

where \bar{u}_i is the fluid velocity, ρ is the fluid density, \bar{p} is the fluid pressure, ν is the kinematic viscosity and $D_{ij} = \bar{u}_i \bar{u}_j - \bar{u}_i \bar{u}_j$ is the hybrid turbulent stress, which is denoted in the DDES

model as

$$D_{ij} = \frac{2}{3}k\delta_{ij} - 2\nu_t\tilde{S}_{ij}, \quad (2.3)$$

where k is the turbulent kinetic energy, δ_{ij} is the Kronecker delta, ν_t is the turbulent viscosity and \tilde{S}_{ij} is the symmetric part of the velocity gradient.

As a hybrid Reynolds-averaged Navier-Stokes (RANS)/LES model, the DDES model takes advantage of both the RANS model and the LES model. The RANS/LES model reduces the computational cost in the boundary layer region around the blades and nozzle compared with LES and has higher computational accuracy than the RANS model in simulating the wake. Compared with the original DES model (Shur *et al.* 1999), the DDES model addresses ambiguous grid densities and more accurately simulates the near-wall flow and wake vortex structures.

The DDES model accurately predicts turbulence near the wall using a one-equation eddy viscosity model, namely, the Spalart–Allmaras (S-A) model (Spalart & Allmaras 1992). The ‘trip function’ with the f_{t2} term in the original S-A model is excluded in the adopted S-A as it only slightly contributes to the fully turbulent computations (Rumsey 2007). The turbulence models are presented in detail by Zhang & Jaiman (2019) and Shi *et al.* (2022).

To simulate the rotation of the blades and hub of the rotor, the arbitrary mesh interface (AMI) approach is employed. This interface approach depends on the super mesh construction algorithm and enables a time-accurate simulation for rotating systems across disconnected and adjacent mesh domains. In the AMI approach, the rotating part covering the blades and hub is implemented inside the computational domain. The rotating and stationary domains are coupled across their interfaces using a conservative interpolation method via the local Galerkin projection proposed by Farrell & Maddison (2011). The governing equations are solved at cell centres in the finite volume domain. The equations for the continuity, momentum, turbulence and rigid body motion are independently solved for the rotor and stator domains.

During the calculations, we adopt a hybrid convection scheme (Travin *et al.* 2002; Spalart *et al.* 2012), which provides a blending between a low dissipative unbounded second-order convection scheme in the LES region and a robust unbounded second-order upwind scheme in the RANS region. The continuity, momentum and turbulence equations are solved by a hybrid solver, which combines the time-accurate pressure implicit with the splitting of operators (PISO) and the semi-implicit method for pressure-linked equations (SIMPLE) algorithms. Temporal discretization is achieved by the backwards-difference scheme with a second-order convergence. Linear equations resulting from the discretized equations are computed using Gauss-Seidel and generalized geometric-algebraic multigrid (GAMG) solvers. All simulations are conducted using open-source computational fluid dynamics (CFD) software: open-source field operation and manipulation (OpenFOAM[®]v2112).

2.2. Numerical setup

The wake dynamics of a four-bladed, fixed-pitch, right-handed propeller (S5810 R) with and without a nozzle (1393 type 19A) operating in axisymmetric and oblique flows are compared in this study. The propeller and nozzle models are chosen because they are designed to eliminate the undesirable hub vortex (Cozijn *et al.* 2010; Cozijn & Hallmann 2012; Maciel *et al.* 2013; Koop *et al.* 2017) and allow us to investigate wake destabilization in the absence of hub vortex interference. Figures 2(a) and 2(b) show the geometries of the models. The parameters of the propeller and nozzle are listed in table 1. The rotor rotational speed, i.e. shaft frequency f_{shaft} , is fixed at $n = 17.65$ rps (revolutions

Effects of a nozzle on the propeller wake

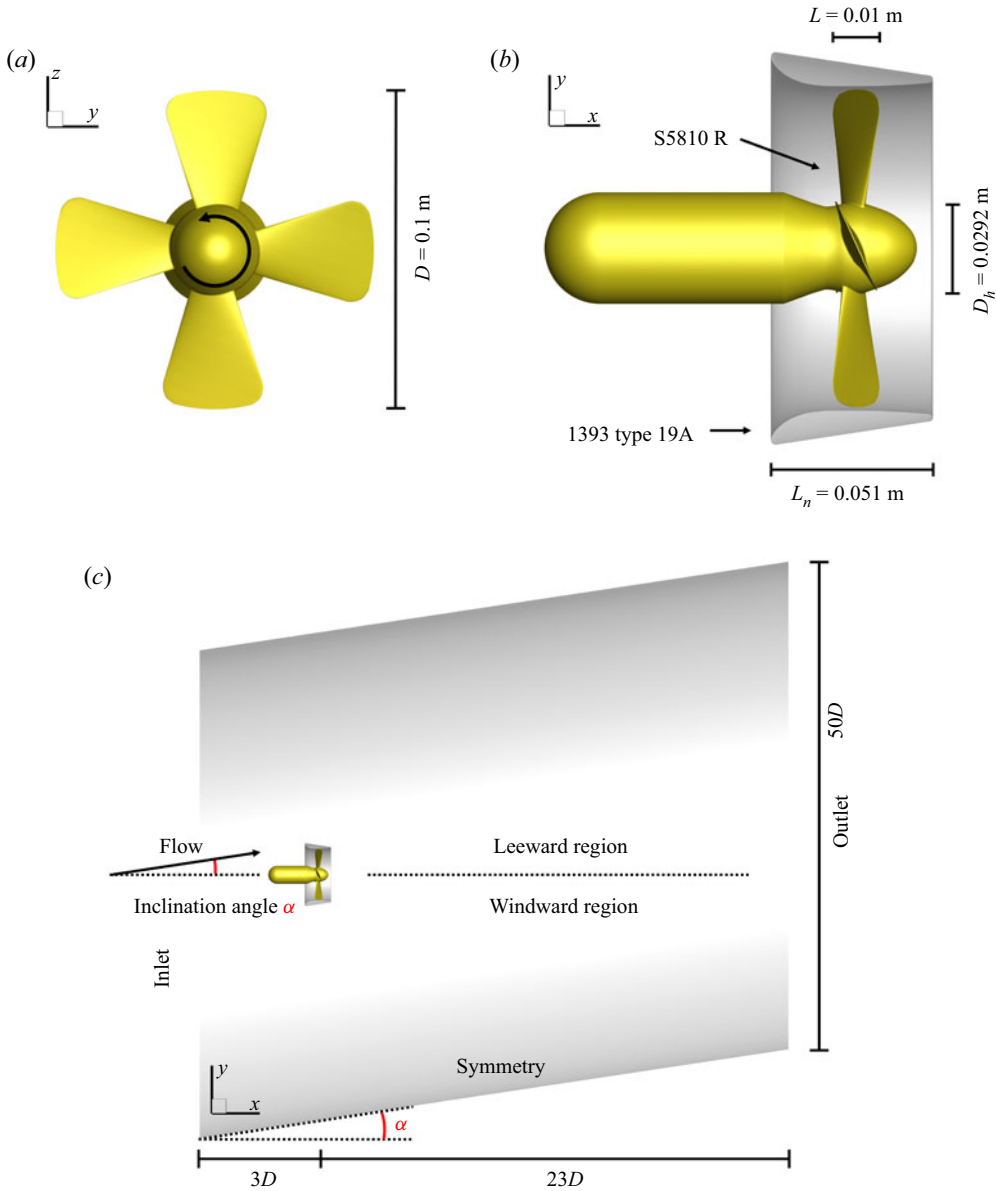


Figure 2. (a,b) Geometries and (c) computational domain of the NP and DP cases. The displayed computational domain is out of proportion. (a) Front view, (b) side view and (c) side view of computational domain.

per second). The Reynolds number based on the rotational speed is $Re_n = nD^2/\nu = 1.765 \times 10^5$, where $D = 0.1$ m is the propeller diameter. The model parameters, rotational speed and Reynolds number are chosen to match previous experimental settings (Cozijn *et al.* 2010; Cozijn & Hallmann 2012) and numerical settings (Maciel *et al.* 2013; Koop *et al.* 2017).

The numerical simulations cover five flow oblique angles $\alpha = 0^\circ, 15^\circ, 30^\circ, 45^\circ$ and 60° for the NP and DP (figure 2c shows the definition of α), totalling ten cases, with a

Parameters	Unit	Value
Propeller diameter (D)	m	0.1
Blade number (Z)	—	4
Blade axial length (L)	m	0.01
Pitch ratio (P/D)	—	1.00
Hub diameter ratio (D_h/D)	—	0.292
Nozzle axial length ratio (L_n/L)	—	5.1

Table 1. Propeller (S5810 R) and nozzle (1393 type 19A) parameters (Maciel *et al.* 2013).

moderate advance coefficient $J = U_\infty/nD = 0.4$, where $U_\infty = (U_{x\infty}^2 + U_{y\infty}^2 + U_{z\infty}^2)^{0.5}$ is the inflow velocity. Using the inflow velocity U_∞ as the reference velocity does not apply to zero inflow velocity conditions, such as dynamic positioning systems or the moment the ship initiates in still water (Zhang & Jaiman 2019). Furthermore, the inflow velocity in the x direction $U_{x\infty} = U_\infty \cos \alpha$ (effective velocity aligned with the propeller axis) is unsuitable for the zero inflow velocity or high inflow angle (e.g. $\alpha = 90^\circ$) case. Therefore, the reference velocity for all cases in this paper is defined according to the blade tip velocity as $U_{tip} = n\pi D \approx 5.54 \text{ m s}^{-1}$ for comparison purposes.

The computational domain is initially a round cylinder with a length of $26D$ and a diameter of $50D$ for zero inflow angle conditions. The computational domain is deformed according to the inflow angle (figure 2c) to anchor the wake to the core (grid encryption zone) of the computational domain and is sheared to ensure a consistent length of the domain in the x direction. The domain extends $3D$ upstream and $23D$ downstream of the NP or DP, and the blockage ratio $\varepsilon = A_d/A_c = 0.0004$ (where A_d is the area of the propeller disk and A_c is the area of the domain's cross-section) is substantially less than the rule of thumb ($\varepsilon < 0.1$) suggested by Kumar & Mahesh (2017) for a blockage effect-free solution.

The boundary conditions of the computational domain are specified as follows. The cylindrical boundary is set as a symmetry condition, and a no-slip boundary condition is specified at the solid surfaces of the propeller and nozzle. The velocity inlet (uniform velocity $U_\infty = 0.706 \text{ m s}^{-1}$ with varying inclination angles) and pressure outlet boundary conditions are prescribed at the left inlet and right outlet of the computational domain.

The central part of the computational domain indicated in figure 2(c) is discretized by Pointwise[®] software into regular and smooth structured meshes. We strictly follow OpenFOAM and Pointwise mesh generation guidelines on skewness and minimum included angle to improve the mesh quality. Three different grid densities, i.e. coarse, medium and fine meshes, are used to conduct a grid sensitivity study in § A.1, and the fine mesh is chosen in this study (the mesh numbers are detailed in table 2). The surface mesh of the NP and DP is shown in figure 3. For each mesh configuration, the y^+ value at the solid surfaces of the NP and DP is below 5, with only a few exceptions (approximately 20 cells) located at blade tips.

Using the steady flow solution calculated by the traditional multiple reference frame (MRF) method as the initial condition, the transient wake evolution is solved using the AMI dynamic mesh. The time step of the transient simulation is $1.575 \times 10^{-5} \text{ s}$, which is the time for the propeller to rotate 0.1 degrees. The wake is fully developed and stabilized after 15 propeller revolutions. For each case, ten (16th–25th) revolutions of flow field data are recorded at an interval of 3 degrees of propeller rotation ($\Delta t = 4.725 \times 10^{-4} \text{ s}$), totalling 1200 snapshots.

Effects of a nozzle on the propeller wake

Cases		Rotor (million)	Stator (million)	Total (million)
NP	$\alpha = 0^\circ$	1.43	40.51	41.94
	$\alpha = 15^\circ$		32.63	34.06
	$\alpha = 30^\circ$		32.55	33.98
	$\alpha = 45^\circ$		32.42	33.85
	$\alpha = 60^\circ$		31.43	32.86
DP	$\alpha = 0^\circ$		31.48	32.91
	$\alpha = 15^\circ$		33.42	34.85
	$\alpha = 30^\circ$		33.09	34.52
	$\alpha = 45^\circ$		32.88	34.31
	$\alpha = 60^\circ$		38.24	39.67

Table 2. Fine meshes were used for each case.

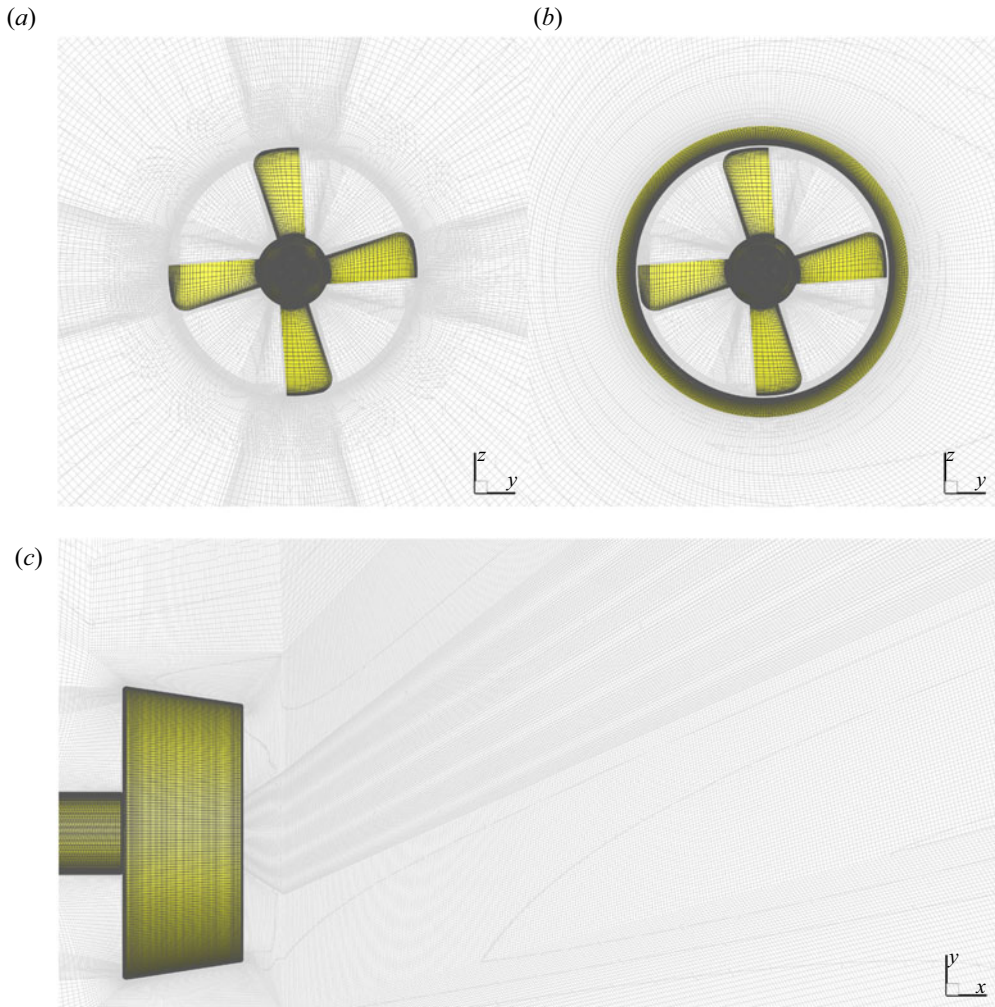


Figure 3. Fine computational mesh near (a) the NP and (b,c) DP. (a) NP front view, (b) DP front view and (c) DP $\alpha = 60^\circ$, side view.

3. Wake field analysis

This section discusses the differences in the wake evolution and destabilization mechanisms between the NP and DP in an oblique flow ($\alpha = 15^\circ, 30^\circ, 45^\circ$ and 60°) based on the instantaneous vorticity magnitude $\Omega = (\Omega_x^2 + \Omega_y^2 + \Omega_z^2)^{0.5}$. Subsequently, the deflection angles of various vortex systems are quantified to determine the effect of the nozzle on the propeller wake deflection.

Figure 4 shows the volume rendering of instantaneous vorticity that displays semitransparent volumetric objects according to the vorticity value and figure 5 shows contours of instantaneous vorticity on the xy plane. According to the degree of instability, the outer portion of the NP and DP slipstream (slipstream is the high-speed stream past the rotor) is divided into three regions: the near-wake region, transition region and far-wake region. The near-wake region is close to the propeller disk, where helices (tip vortices for the NP and tip leakage vortices for the DP) have well-defined helical morphology. The region where the helices couple with other vortex systems and lose their original morphology is defined as the transition region. The far-wake region is where the helices are broken down into small-scale, disordered turbulence. The three regions are separated by red and yellow dashed lines in figure 4.

The key findings in this section are the formation of a tube-shaped wake envelope (referred to as the vortex tube) and its subsequent rolling-up in the wake of the DP in an oblique inflow (figure 6). The generation mechanism of the vortex tube is ascribable to the similar vorticity intensity/magnitude between the helices and the secondary vortices, which are discussed in detail below.

3.1. Vortex interaction mechanisms

This subsection focuses mainly on the destabilization mechanisms of the helices in the outer slipstream. For illustration purposes, ten cases are classified into two groups: Group 1 includes NP at $\alpha = 0^\circ, 15^\circ, 30^\circ, 45^\circ$ and 60° , and DP at $\alpha = 0^\circ$; Group 2 includes DP at $\alpha = 15^\circ, 30^\circ, 45^\circ$ and 60° . The destabilization mechanisms in the outer slipstream of the two groups have significant differences.

Under axisymmetric conditions, tip vortices of the NP have a symmetric vorticity intensity and vortex core size/radius with respect to the propeller axis (figure 5a). When the propeller is confined in a nozzle (i.e. DP configuration), the nozzle exerts a shear on the tip vortices that leak from the gap between the blade tip and the nozzle, and the resulting tip leakage vortices undergo a vorticity redistribution on the nozzle inner sidewall (Gong *et al.* 2018; Shi *et al.* 2022), as shown in figure 5(b). Therefore, in an axisymmetric flow, the vorticity intensity of NP tip vortices is significantly higher than that of DP tip leakage vortices. For the NP in an oblique flow, time-dependent shed vortices and inhomogeneous blade circulation cause an asymmetric vortex core size of helices, and the vortex core size is larger in the windward region than in the leeward region (figure 5c,e,g,i).

In the near-wake region of Group 1, the interaction between the trailing edge vortices and the helices destabilizes the outer slipstream. As documented by Shi *et al.* (2022), the convection velocity of the trailing edge vortices is faster than that of the helices; as a result, each trailing edge vortex disconnects from its corresponding helix and moves towards the downstream, previously shed helices.

The torsion exerted on the helices by the trailing edge vortices plays a crucial role in the short-wave instability of helices, as highlighted by Ricca (1994), Ahmed, Croaker & Doolan (2020), Gong *et al.* (2021) and Shi *et al.* (2022). During the interaction between the trailing edge vortices and the helices, the vortex filaments in the helices are

Effects of a nozzle on the propeller wake

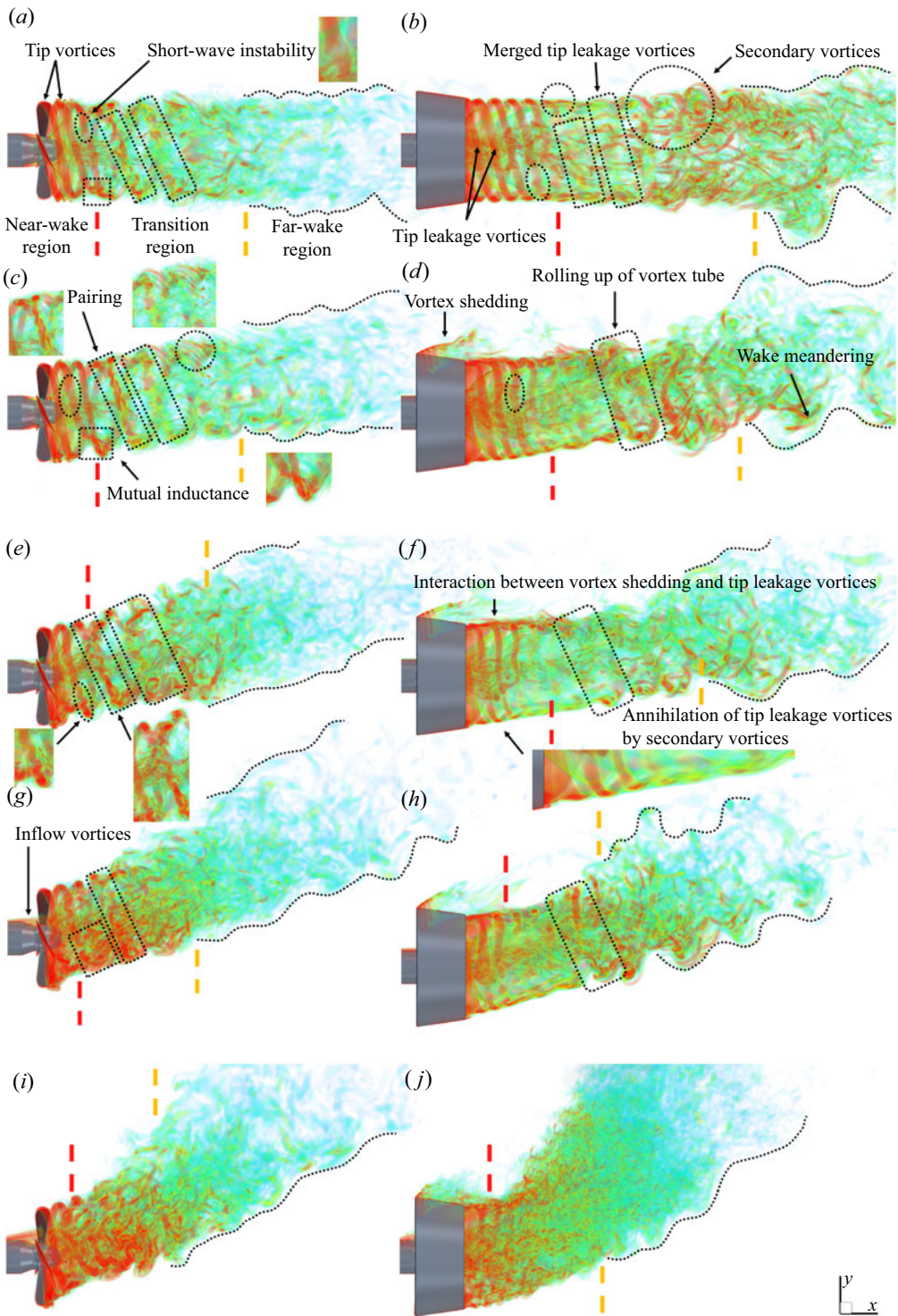


Figure 4. Volume rendering of the normalized instantaneous vorticity magnitude $\Omega D/U_{tip}$ for the NP at (a) $\alpha = 0^\circ$, (c) 15° , (e) 30° , (g) 45° and (i) 60° , and the DP at (b) $\alpha = 0^\circ$, (d) 15° , (f) 30° , (h) 45° and (j) 60° . The three regions are separated by red and yellow dashed lines.

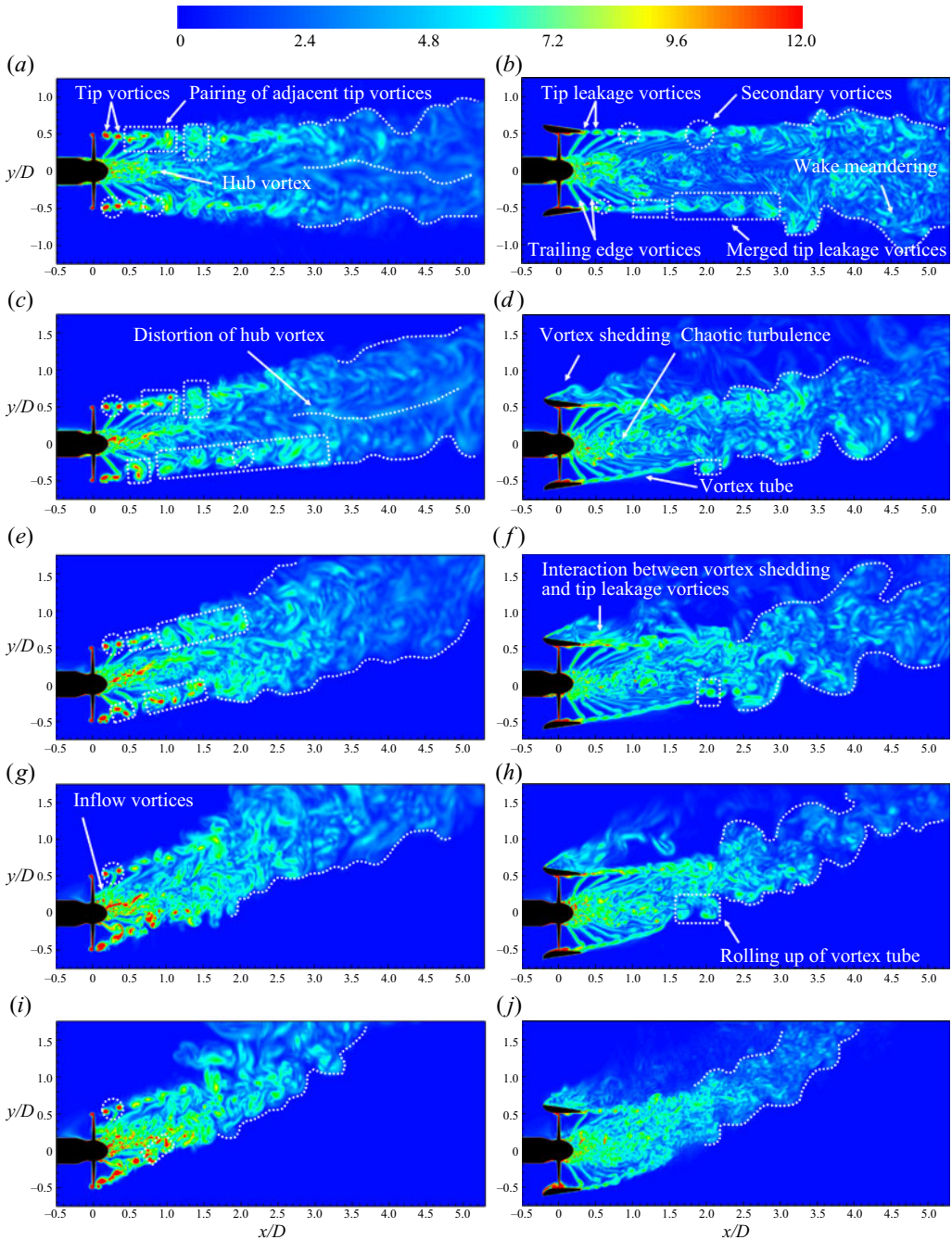


Figure 5. Contours of instantaneous vorticity magnitude Ω for the NP at (a) $\alpha = 0^\circ$, (c) 15° , (e) 30° , (g) 45° and (i) 60° , and the DP at (b) $\alpha = 0^\circ$, (d) 15° , (f) 30° , (h) 45° and (j) 60° . The vorticity is normalized by U_{tip}/D .

ripped out by the trailing edge vortices, and consequently, the helices undergo short-wave instability (areas enclosed by ellipses in figure 4a,b,c,e,g,i). Simultaneously, the trailing edge vortices shift the vortex filaments from the upstream helices to the downstream

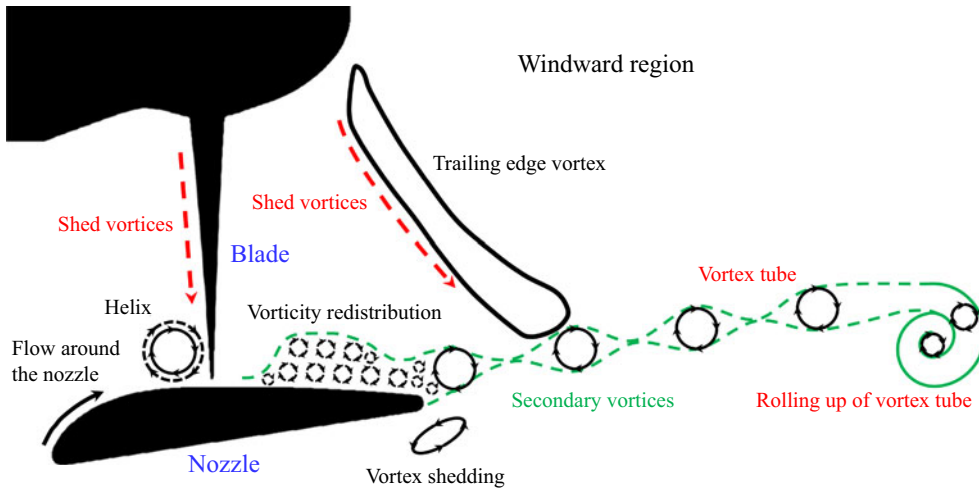


Figure 6. Schematic of the formation of a vortex tube and its rolling-up for the DP in an oblique flow.

helices, forming secondary vortices between adjacent helices (areas enclosed by circles in figure 5*a,b,c,e,g,i*).

The secondary vortices enhance the mutual inductance between adjacent helices, and consequently, two adjacent helices begin to pair/merge (rectangular boxes in figures 4*a,b,c,e,g,i* and 5*a,b,c,e,g,i*). In the transition region of Group 1, the dominant wake destabilization mechanism in the outer slipstream is helix pairing (Felli *et al.* 2011), which subsequently produces merged helices (marked by rectangular boxes with rounded corners in figures 4*a,b,c,e,g,i* and 5*a,b,c,e,g,i*). The merged helices are extremely unstable, with strong secondary vortices between them.

The generation mechanisms of secondary vortices are different in the near-wake and transition regions of Group 1. In the near-wake region, the secondary vortices are essentially vortex filaments ripped out by the trailing edge vortices from the helices. However, in the transition region, the trailing edge vortices are gradually broken down due to viscous dissipation, and the secondary vortices are dominated by the shear exerted by the free stream on the merged helices, consistent with the findings of Di Mascio *et al.* (2014).

In Group 2, vortex shedding is defined as the phenomenon of flow separation from the nozzle as a result of the yawed misalignment. In figure 5(*d,f,h,j*), the vortex shedding from the leeward nozzle leading edge is stronger than that from the windward nozzle leading edge (significant only for the DP at $\alpha = 60^\circ$, as shown in figure 5*j*) and trailing edges.

In an oblique flow, the helices of DP have a vorticity intensity similar to the secondary vortices due to the shear and vorticity redistribution experienced by the helices on the nozzle inner sidewall. In the near-wake region of Group 2, the coupling between the helices and the secondary vortices forms a coherent tube-shaped wake envelope (i.e. a vortex tube that separates the undisturbed flow from the slipstream, as shown in figure 5*d,f,h,j*), that is, the vortex tube is formed by a helix frame covered by secondary vortices.

The formation mechanisms of the vortex tube are different in the windward and leeward regions of Group 2. Figure 6 illustrates the four mechanisms that contribute to the generation of secondary vortices in the windward region: (i) the interaction between the trailing edge vortices and the helices; (ii) the disturbance of the time-dependent shed vortices on helix formation and vorticity redistribution; (iii) the interference of

the vortex shedding from the windward nozzle leading edge on the helix formation and vorticity redistribution, which is significant only for the DP at $\alpha = 60^\circ$ (figure 5j); (iv) the interaction between the vortex shedding from the windward nozzle trailing edge and the helixes. In the leeward region of Group 2, in addition to mechanisms (i) and (ii), another decisive trigger to form the vortex tube is (v) the strong interaction between the vortex shedding from the leeward nozzle leading edge and the helixes, as illustrated in figures 4(d,f,h,j) and 5(d,f,h,j).

Since the vortex tube has been formed in the near-wake region of Group 2 due to the strong interaction among helixes, shed vortices and vortex shedding, the helix pairing phenomenon is invisible in the transition region. Instead, the rolling-up of the vortex tube is a new destabilization mechanism in the transition region of Group 2, especially in the windward region, as marked by rectangular boxes with rounded corners in figures 4(d,f,h,j) and 5(d,f,h,j). The rolling-up of the vortex tube in the present study is similar to the generation mechanism of vortex rings at the nozzle exit (Allen & Auvity 2002; Le *et al.* 2011; Steinfurth & Weiss 2020). The difference between them is that the former is a secondary instability process because the vortex tube consists of helixes and secondary vortices, but the latter is a primary process. During the downstream convection, the vortex tube always rolls up outwards with respect to the inner slipstream, and the rolling-up direction of the vortex tube matches the helix rotation direction (figure 6). Additional analysis of vortex tube rolling-up is provided in § 4.3.2 using modal decomposition techniques.

The trailing edge vortices entirely break down when the wake evolves to the far-wake region. Without the brace of the trailing edge vortices between the inner slipstream and the outer slipstream, the wake is susceptible to wiggling under the shear from the free stream. As a result, in the far-wake region of Groups 1 and 2, the dominant destabilization mechanism in the outer slipstream is wake meandering characterized as large-scale, low-frequency and stochastic (Felli *et al.* 2011; Magionesi *et al.* 2018), as shown in figures 4 and 5.

Wake meandering is a common phenomenon in wind farms (Kang *et al.* 2014; Howard *et al.* 2015; Viola *et al.* 2015; Bastankhah & Porté-Agel 2016, 2017; Foti *et al.* 2016; Foti *et al.* 2018a,b; Mao & Sørensen 2018; Gupta & Wan 2019; Li & Yang 2021), but its generation mechanism is still not fully understood. For the wind turbine and propeller wake, some previous investigations hypothesized that global meandering is ascribed to hub vortex distortions (Felli *et al.* 2011; Iungo *et al.* 2013; Viola *et al.* 2014; Howard *et al.* 2015; Ashton *et al.* 2016). However, without modelling a hub vortex, Mao & Sørensen (2018) and Foti *et al.* (2018a) found that stochastic wake meandering is driven by shear from the free stream and is dominated by large-scale vortices with helical morphology. Unfortunately, it is difficult to identify the generation mechanism of wake meandering via traditional flow visualization methods. Instead, modal decomposition techniques are employed to investigate the wake meandering mechanism in depth in § 4.3.4.

In the internal portion of the slipstream, the hub vortex is observed near the hub of the NP in axisymmetric and oblique flow conditions, as shown in figure 5(a,c,e,g,i). The hub vortex is formed by the coalescence of root vortices shed from the blade roots and the shear layers detached from the hub under the propeller rotation (Felli & Falchi 2018). However, the NP hub vortex is weak in this study, and additionally, the centrifugal effect of the DP nozzle further breaks down the weak hub vortex into chaotic turbulence (figure 5b,d,f,h,j). The breakdown of the hub vortex gives us a chance to investigate the far-wake meandering phenomenon without interference from hub vortex distortions.

For both the NP and DP in an oblique flow, the vortices shed from the propeller stem are referred to as inflow vortices, consistent with the findings of Felli & Falchi (2018). The inflow vortices are strong in the wake of the NP and DP when the inflow angle $\alpha \geq 45^\circ$ (figure 5g,h,i,j). For the NP, the inflow vortices are coupled with the hub vortex, making it challenging to identify the hub vortex. However, for the DP, the inflow vortices have minimal effects on the fully destabilized chaotic turbulence.

3.2. Quantitation analysis of the wake deflection angle

An oblique flow significantly deflects the alignment angle of various vortex systems in the wake of the NP and DP. The deflection angles of wake vortices are different in the windward and leeward regions, and the hub vortex in the NP wake centre also has a distinct deflection angle. The deflection angle of each vortex system is determined based on the phase-averaged vorticity on the xy plane shown in figure 7. In figure 8, the locations of well-defined and merged helices in the windward and leeward regions of the NP and DP wakes are mapped on the xy plane, and a linear fit is used to evaluate the deflection angle of the outer slipstream based on the locations of these well-defined and merged helices. Note that NP helix 0 and DP helices 0 to 2 in figures 7 and 8 are not considered in the linear fit because they are newly formed and unstable.

Figure 9 shows the variations in the deflection angles of the hub vortex β_h , and the windward β_w and leeward β_l outer slipstream with inflow angle α . For both the NP and DP in an oblique flow, the deflection angle of the outer slipstream is greater on the windward side than on the leeward side, as shown in figure 9(a). On the windward side, the deflection angle of the NP outer slipstream is higher than that of the DP outer slipstream at the same inflow angle when $\alpha \geq 30^\circ$. Similarly, on the leeward side, the deflection angle of the DP outer slipstream is almost zero, and the deflection angle of the NP outer slipstream is always higher than that of the DP outer slipstream at the same inflow angle. For the NP in an oblique flow, the deflection angle of the hub vortex is always higher than that of the leeward outer slipstream, which implies that the hub vortex tends to penetrate the leeward outer slipstream. The deflection angle of the hub vortex at NP $\alpha = 60^\circ$ is not considered because the inflow vortices from the propeller stem severely disturb the inner slipstream (figure 7i).

The angle deviation between the inflow angle α and the deflection angle β is defined as the deviation angle, $\alpha - \beta$, which is positively correlated with the resistance of the wake against the inclined inflow. The deviation angle in figure 9(b) implies that oblique flow has a minimal effect on the leeward outer slipstream of the DP. Conversely, the windward outer slipstream of the DP, the windward and leeward outer slipstream of the NP, and the hub vortex of the NP are susceptible to deflection in an oblique flow, but their resistance against the oblique flow enhances with increasing inflow angle.

According to figure 7, for the NP and DP in an oblique flow, the deflection angle of the outer slipstream is different on the windward and leeward sides, so the fitted lines on the two sides necessarily have an intersection point in the wake region. Here, the line between the intersection point and the origin (0, 0) is defined as the nominal wake centre (different from the hub vortex) to measure the deflection of the overall wake (main flow), and the deflection and deviation angles of the nominal wake centre are reported in figure 9(c). The deflection angle of the NP and DP main flow follows approximately a linear function with the inflow angle, and the nozzle can effectively weaken the wake deflection in an oblique flow. In general, the resistance of the wake against the oblique flow can be ascribed to the following four factors: (i) shelter effect of the nozzle against

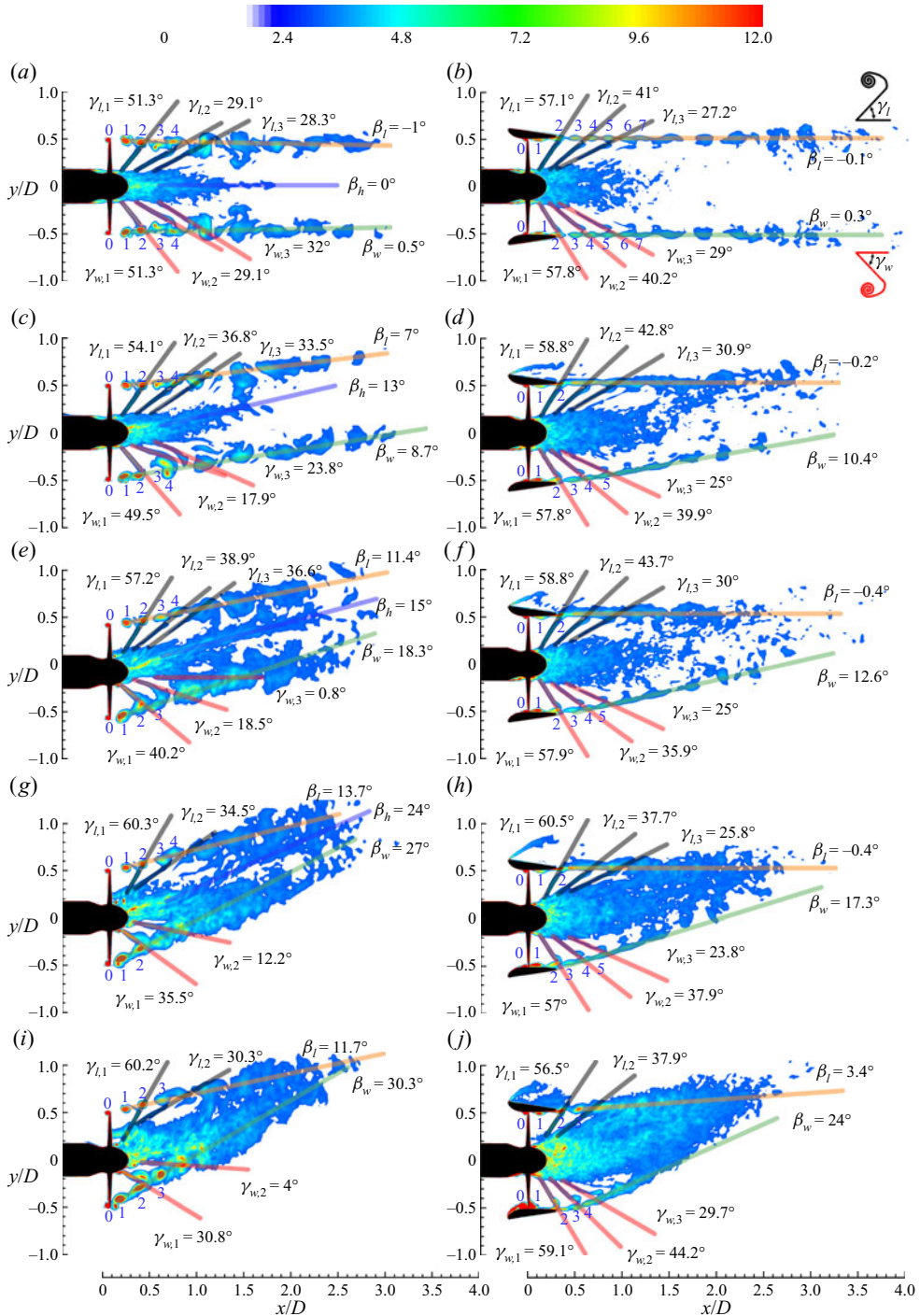


Figure 7. Contours of phase-averaged vorticity magnitude Ω for the NP at (a) $\alpha = 0^\circ$, (c) 15° , (e) 30° , (g) 45° and (i) 60° , and the DP at (b) $\alpha = 0^\circ$, (d) 15° , (f) 30° , (h) 45° and (j) 60° . The vorticity is normalized by $U_{tip}D$. The well-defined helices marked by blue numbers are mapped on the xy plane in figure 8. Here, β_h , β_w and β_l denote the deflection angle of the hub vortex, windward outer slipstream and leeward outer slipstream, respectively, as reported in figure 9; γ_w and γ_l defined in figure 9(b) denote the hydrodynamic pitch angle of the windward trailing edge vortex and leeward trailing edge vortex, respectively, as reported in figure 10.

Effects of a nozzle on the propeller wake

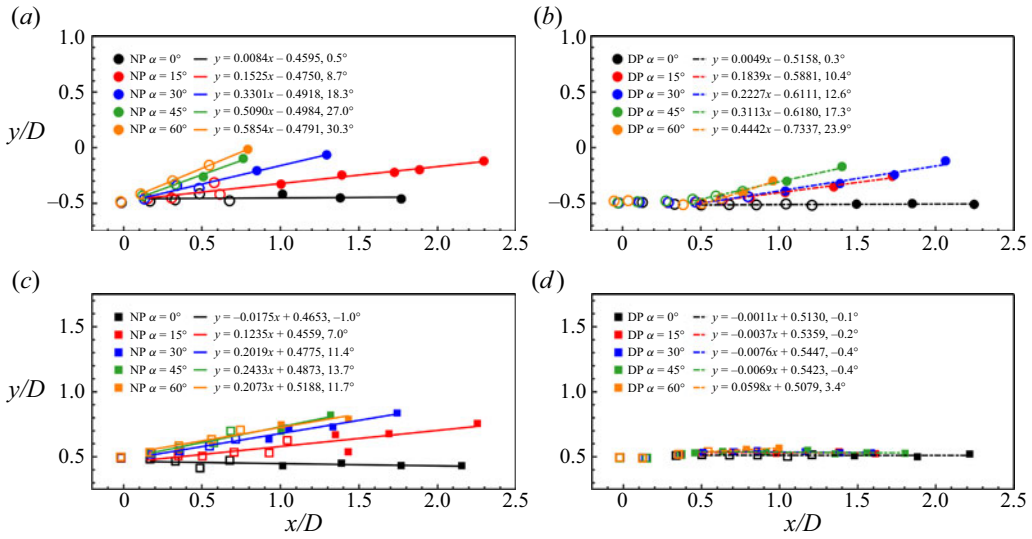


Figure 8. Locations of the well-defined helices (unfilled markers) and merged helices (filled markers) on the (a,b) windward side and (c,d) leeward side of the NP and DP at $\alpha = 0^\circ, 15^\circ, 30^\circ, 45^\circ$ and 60° . Linear fits are used to evaluate the deflection angle of the outer slipstream. (a) NP windward, (b) DP windward, (c) NP leeward and (d) DP leeward.

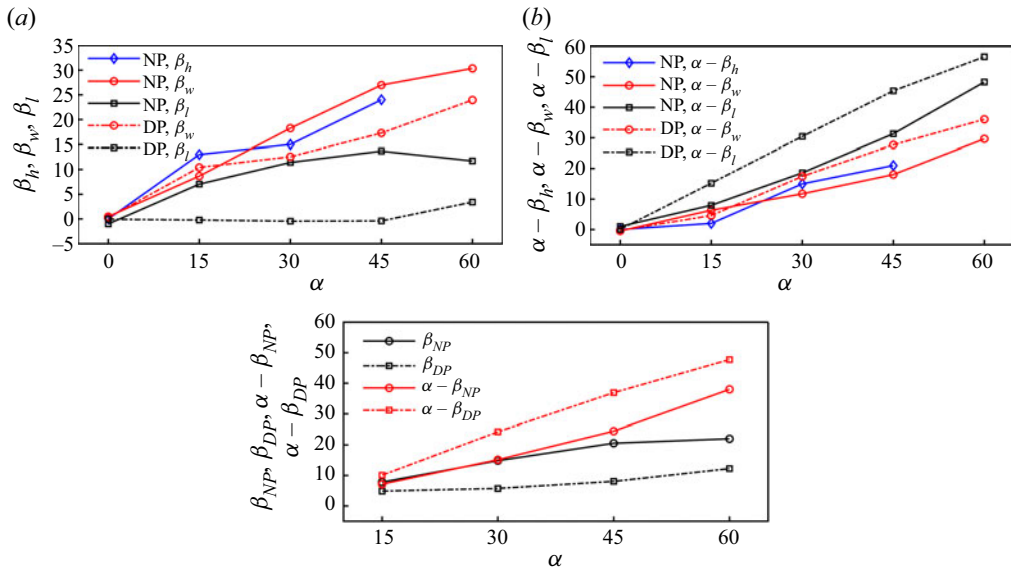


Figure 9. Inflow angle versus the (a) deflection angle and (b) deviation angle of the hub vortex and outer slipstream on the windward and leeward sides of the NP and DP at $\alpha = 0^\circ, 15^\circ, 30^\circ, 45^\circ$ and 60° . (c) Inflow angle versus the deflection and deviation angles of the NP and DP wake centre.

oblique inflow; (ii) acceleration delivered by the propeller rotation; (iii) fluid viscosity; (iv) brace of the trailing edge vortices between the inner slipstream and the outer slipstream, as mentioned by Felli & Falchi (2018).

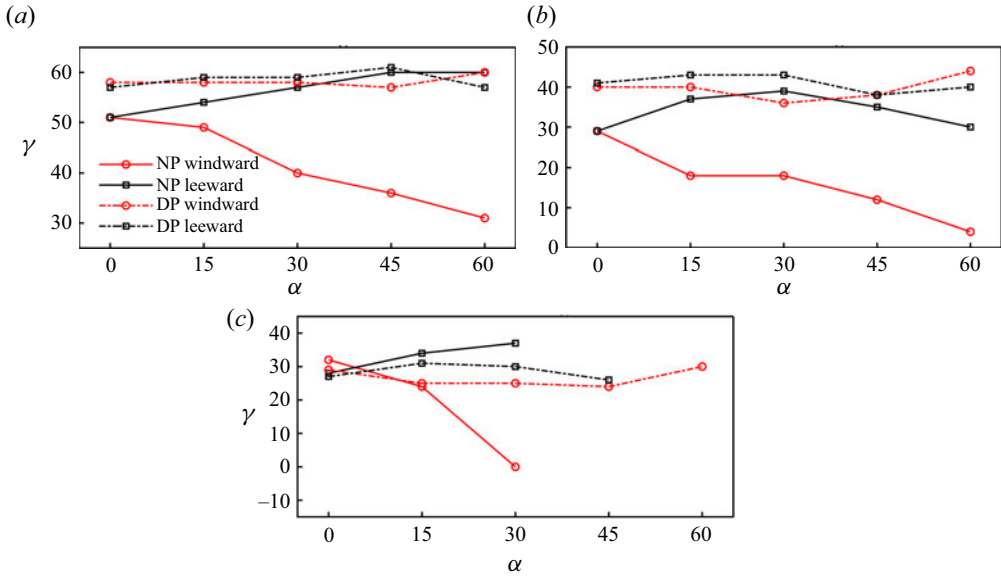


Figure 10. Inflow angle versus the hydrodynamic pitch angle of the (a) first, (b) second and (c) third trailing edge vortices on the windward and leeward sides of the NP and DP at $\alpha = 0^\circ, 15^\circ, 30^\circ, 45^\circ$ and 60° .

In figure 7, an oblique flow also affects the hydrodynamic pitch angle γ of the trailing edge vortices (figure 7b), and the pitch angle of the first three unbroken trailing edge vortices is measured in figure 10. In the windward (leeward) region, the pitch angle is expected to decrease (increase) with increasing inflow angle due to wake deflection. However, for both the NP and DP, the inflow vortices that are shed from the propeller stem severely disrupt the inner slipstream and alter the pitch angle of the trailing edge vortices, especially when $\alpha \geq 45^\circ$ (figure 7).

The interference of the inflow vortices on the pitch angle of the trailing edge vortices is insignificant only in the NP windward region, where the pitch angles of the first three trailing edge vortices monotonically decrease with increasing inflow angle, with maximum variations of 20, 25 and 32 degrees for the first, second and third trailing edge vortices, respectively. For the first three trailing edge vortices in the NP leeward region, their variations in pitch angle with inflow angle are within 10 degrees, which is relatively moderate compared to the variations in the NP windward region. For the DP, under the shelter of the nozzle, the pitch angles of the first three trailing edge vortices in both the windward region and leeward region are insensitive to the inflow angle.

The velocity magnitude $U = (U_x^2 + U_y^2 + U_z^2)^{0.5}$ is a desirable quantity to illustrate the velocity characteristics of various vortex systems as it is independent of the inflow angle and can show the differences in the deflection angle and value of the wake velocity for various cases. Figure 11 shows the profiles of the time-averaged velocity U along the lines of $x/D = 0.4, 0.7, 1, 1.5, 2, 2.5$ and 3 on the xy plane to evaluate the effects of an oblique flow on the wake velocity of the NP and DP.

In the axisymmetric condition with $\alpha = 0^\circ$, the minimum velocity of the NP and DP wakes is always in the hub region of the propeller $y/D = 0$. Within $1D$ downstream of the propeller disk ($x/D < 1$), the maximum velocity of the NP wake at $\alpha = 0^\circ$ is approximately $|y/D| = 0.4$, and this radial position moves outward to approximately $|y/D| = 0.45$ when the nozzle is mounted around the propeller, i.e. DP $\alpha = 0^\circ$. In figure 7(a,b), the helices

Effects of a nozzle on the propeller wake

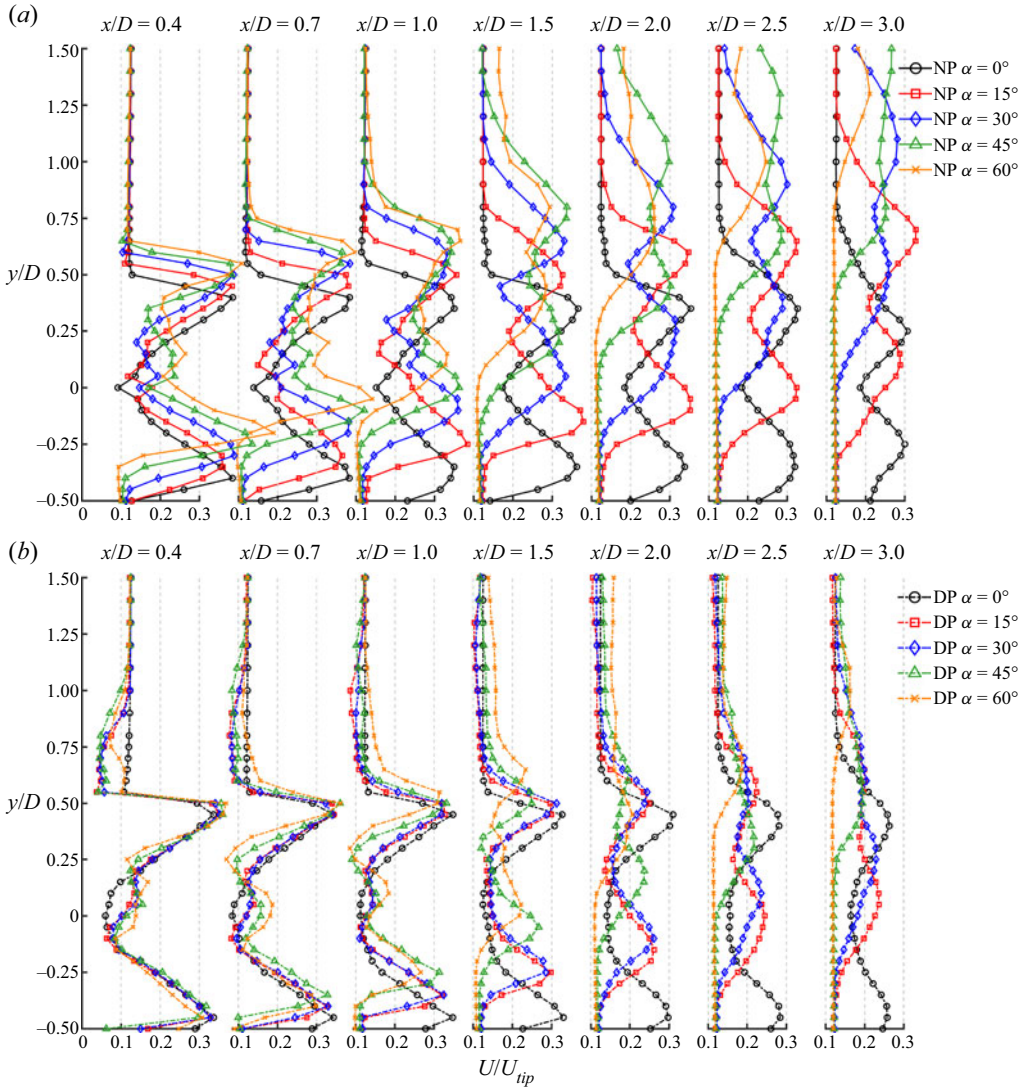


Figure 11. Profiles of time-averaged velocity magnitude U of the (a) NP and (b) DP at $\alpha = 0^\circ, 15^\circ, 30^\circ, 45^\circ$ and 60° . The profiles are located at $x/D = 0.4, 0.7, 1, 1.5, 2, 2.5$ and 3 on the xy plane. The velocity is normalized by U_{tip} .

are located at approximately $|y/D| = 0.5$ for both the NP and DP at $\alpha = 0^\circ$, and $|y/D| = 0.4$ for the NP or 0.45 for the DP corresponds to the ends of the trailing edge vortices. The difference in the velocity value between $|y/D| = 0.5$ and $|y/D| = 0.4$ or 0.45 explains the destabilization mechanism that each trailing edge vortex interacts with the downstream, previously shed helices, as detailed in § 3.1. Further downstream ($x/D \geq 1$), the maximum velocity of the NP wake progressively shrinks towards the internal portion of the wake, but that of the DP wake is always at $|y/D| = 0.45$, which implies that the presence of the nozzle can inhibit the slipstream contraction behaviour (Felli *et al.* 2011; Di Mascio *et al.* 2014). Moreover, the nozzle reduces the wake velocity. Using the line of $x/D = 0.4$ at $\alpha = 0^\circ$ as an example, the minimum velocity in the hub region of the wake is $U/U_{tip} = 0.09$ for the

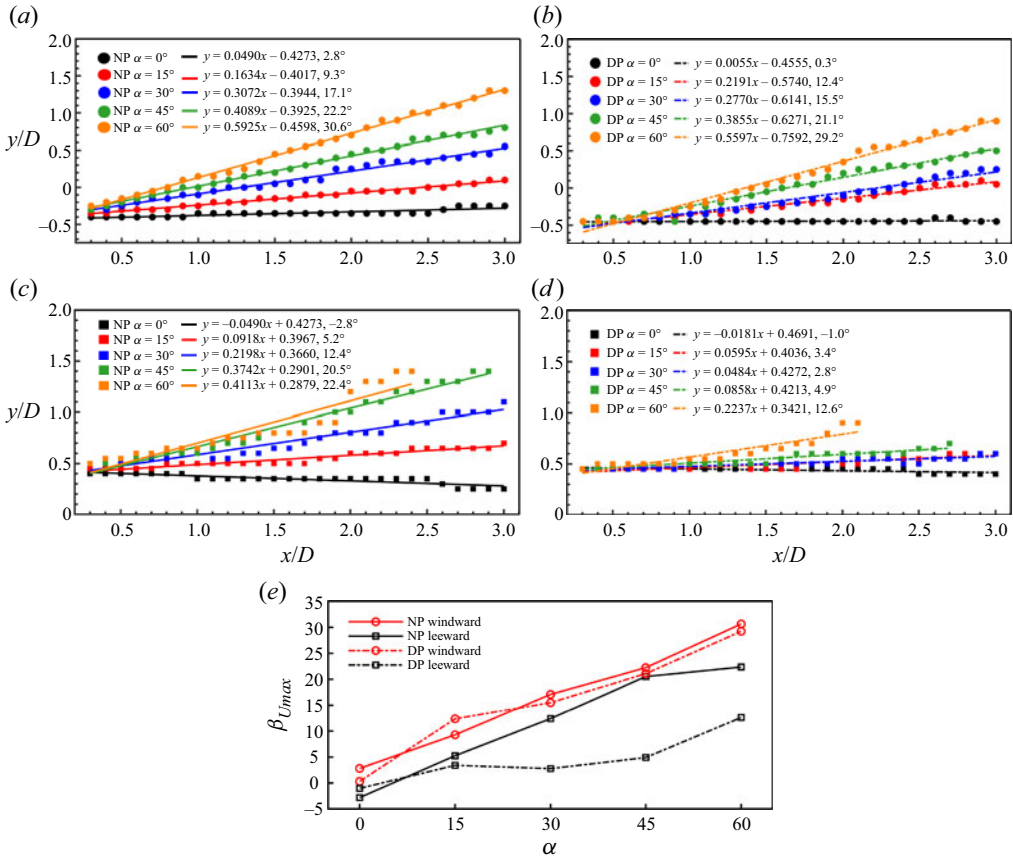


Figure 12. Locations of the peaks of time-averaged velocity magnitude U on the (a,b) windward side and (c,d) leeward side of the NP and DP at $\alpha = 0^\circ, 15^\circ, 30^\circ, 45^\circ$ and 60° . A linear fit is applied to evaluate the deflection angle of the velocity peak. (e) Inflow angle versus the velocity peak deflection angle. (a) NP windward, (b) DP windward, (c) NP leeward, (d) DP leeward and (e) statistics.

NP and $U/U_{tip} = 0.06$ for the DP, and the maximum velocity is $U/U_{tip} = 0.39$ for the NP and $U/U_{tip} = 0.34$ for the DP.

When the inflow is inclined, the oblique flow deflects the wake and alters the radial position and value of the maximum velocity. In figure 12(a-d), the locations of the local maximum velocity on the windward and leeward sides of the NP and DP wakes from $x/D = 0.3$ to 3 are mapped on the xy plane with the profiles spaced at $x/D = 0.1$. The alteration of the local maximum velocity's radial positions during the downstream convection is illustrated by the deflection angle of the maximum velocity $\beta_{U_{max}}$, which is obtained by linear curve fitting of the data in figure 12(a-d). The variation in the deflection angle $\beta_{U_{max}}$ with inflow angle α is reported in figure 12(e). The evolution of the minimum wake velocity is not discussed as the strong flow coupling in the hub region of the wake makes it difficult to define the minimum velocity in each profile.

For both the NP wake and DP wake, the deflection angle $\beta_{U_{max}}$ on the windward side is higher than that on the leeward side due to the direct interaction of the windward wake with the oblique flow. Moreover, compared with the deflection angle $\beta_{U_{max}}$ on the NP leeward side, the shelter effect of the nozzle significantly reduces the deflection angle $\beta_{U_{max}}$ on the DP leeward side, especially for $\alpha \geq 30^\circ$.

For the value of the maximum velocity, an apparent difference between the NP at $\alpha = 15^\circ$ and 30° and the NP at $\alpha = 45^\circ$ and 60° is observed in [figure 11](#). At $x/D = 0.4$ and 0.7 , the maximum velocity values of the NP at $\alpha = 15^\circ$ and 30° are approximately equivalent to that of the NP at $\alpha = 0^\circ$ on both the windward side and leeward side. As the inclination angle is further increased, on the NP leeward side, the maximum velocity values at $\alpha = 45^\circ$ and 60° approximate those at $\alpha = 0^\circ$, 15° and 30° . However, on the NP windward side, the maximum velocity values at $\alpha = 45^\circ$ and 60° are significantly higher than those at $\alpha = 0^\circ$, 15° and 30° , and the difference in the maximum velocity values increases with increasing inflow angle (as shown in the $x/D = 0.4$ and 0.7 profiles in [figure 11a](#)).

A contrary trend is observed in the DP windward region at $x/D = 0.4$ and 0.7 ([figure 11b](#)). The maximum velocity values in the DP windward region decrease with increasing inflow angle due to the obstruction of the inflow by the nozzle. However, the maximum velocity values in the DP leeward region are still insensitive to the inflow angle, following the same trend as those in the NP leeward region.

4. Modal analysis

In this section, two modal decomposition techniques, proper orthogonal decomposition (POD, Lumley 1970; Sirovich 1987) and dynamic mode decomposition (DMD, Rowley *et al.* 2009; Schmid 2010), are employed to analyse space-frequency information in the NP and DP wakes. Detailed theories of POD and DMD are provided in § A.2.

4.1. Dataset

Both POD and DMD are performed based on the snapshot matrix X , which includes the variable being analysed and the spatial n and temporal m dimensions.

4.1.1. Analysis variable

Our previous study demonstrated that the modes obtained based on the vorticity magnitude can resolve various wake vortex structures and their instability (Shi *et al.* 2022). Thus, the vorticity is still chosen for modal analysis in the present work.

According to Chen, Tu & Rowley (2012) and Tu *et al.* (2014), subtracting the mean data from the dataset allows the POD eigenvalues (square of singular values σ_i^2) to be interpreted as the variance in fluctuations, but it might reduce the DMD to the temporal discrete Fourier transform (DFT). The removal of the mean data would distribute all DMD modes at a uniform frequency interval and disturb the frequencies of non-periodic modes. Therefore, the mean vorticity is retained in the datasets for DMD but is subtracted from the datasets for POD.

4.1.2. Spatial dimension of the snapshot matrix

The mesh number of the computational domain determines the spatial dimension n of snapshots. To reduce the calculation costs, a cylindrical computational subdomain with $7D$ in length ($x/D = -1$ to 6) and $4D$ in diameter ($|z/D| = 0$ to 2 , and $|y/D| = 0$ to 2 for axisymmetric conditions and $y/D = -1$ to 3 for oblique flow conditions) is chosen to ensure that the core flows are contained in the subdomain. Moreover, the dynamic domain contained in the subdomain is not considered as the time delay in the data transmission between the dynamic domain and stationary domain might affect the modal decomposition

Cases		Mesh number (million)
NP	$\alpha = 0^\circ$	15.82
	$\alpha = 15^\circ$	15.84
	$\alpha = 30^\circ$	15.88
	$\alpha = 45^\circ$	15.91
	$\alpha = 60^\circ$	15.97
DP	$\alpha = 0^\circ$	18.51
	$\alpha = 15^\circ$	19.11
	$\alpha = 30^\circ$	19.23
	$\alpha = 45^\circ$	19.29
	$\alpha = 60^\circ$	19.35

Table 3. Mesh number of the computational subdomain for the ten cases.

(Magionesi *et al.* 2018; Shi *et al.* 2022; Wang *et al.* 2022). The mesh numbers of the subdomain for the ten cases are listed in table 3.

4.1.3. Temporal dimension of the snapshot matrix

The snapshot number m in the dataset depends on the snapshot sampling time interval and sampling size. The sampling time interval must be sufficiently small to resolve the high-frequency flows and the sampling size must be sufficiently long to record the low-frequency phenomena. Based on the modal convergence analysis in § A.3, datasets with a sampling time interval of $\Delta t_s = \Delta t = 4.725 \times 10^{-4}$ s and a sampling size of nine propeller revolutions are chosen for modal analysis, with 1080 POD and DMD modes in each case.

4.2. Modal statistics

To select a subset of POD and DMD modes that dominates the wake destabilizations, a sparse selection method is necessary to identify the critical modes. This section will identify the dominant modes according to the POD and DMD spectra.

4.2.1. Energy and spectra of POD modes

Figure 13 shows the relative and cumulative energy of POD modes based on (A3). The relative energy of each mode reflects the spatial information the mode contains, while the convergence rate of the cumulative energy curve is related to flow destabilization. The convergence rate of the energy content of a severely destabilized wake is generally slow because the disordered small-scale turbulence occupies a considerable proportion of the energy content (Magionesi *et al.* 2018; Shi *et al.* 2022). For the NP and DP wakes at $\alpha = 0^\circ, 15^\circ, 30^\circ, 45^\circ$ and 60° , the first 404, 420, 477, 608, 657 modes and 189, 206, 207, 249, 423 modes, respectively, reach 99% of the total modal energy, which indicates that the convergence rate of the cumulative energy decreases with increasing inflow angle (figure 13c,d), but the nozzle of DP can accelerate the energy convergence.

Figure 14 shows the normalized PSD (i.e. POD spectra) obtained by performing the fast Fourier transform on the time coefficient of each POD mode (A2), with the black pixels representing the location of spectral peaks. Only the spectra of the NP and DP at $\alpha = 0^\circ, 45^\circ$ and 60° are shown here. The spectra of the remaining NP and DP cases are similar to the results at $\alpha = 0^\circ$. The non-dimensional frequency is defined as $\kappa = f/f_{shaft} = f/17.65$,

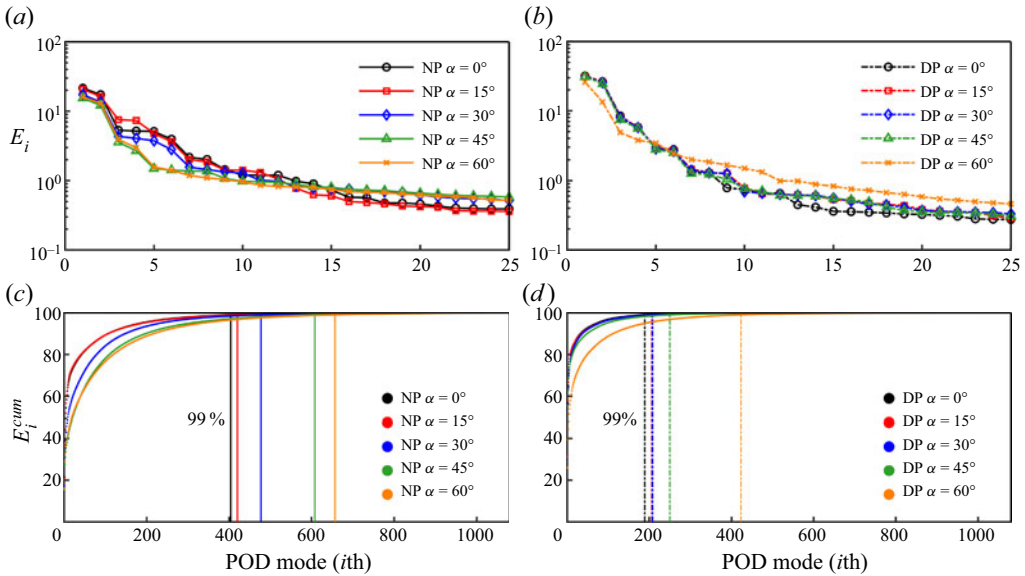


Figure 13. (a,b) Relative and (c,d) cumulative energy of POD modes for the NP and DP cases. (a) NP relative energy, (b) DP relative energy, (c) NP cumulative energy and (d) DP cumulative energy.

where f is the modal frequency and f_{shaft} is the shaft frequency. For the four-bladed rotor, the non-dimensional shaft frequency is denoted by $\kappa = 1$, the half blade frequency is $\kappa = 2$ and the blade frequency is $\kappa = 4$.

For both the NP wake and DP wake, the spectral peaks of the POD modes are linear functions of the modal order. However, the modal order of a few modes dramatically drops away from the diagonal line and moves to the left; this drop is referred to as the ‘jumping-order’, as illustrated by the zoom-in view in figure 14. Shi *et al.* (2022) reported that the jumping order is a characteristic behaviour of dominant POD modes. For the NP wake, the jumping-order modes are characterized by spectral peaks at $\kappa = [2: 2: 60]$ (i.e. $\kappa = 2, 4, 6, \dots, 60$). For the DP wake, the jumping-order behaviour of the modes with spectral peaks at $\kappa = [2: 4: 58]$ (i.e. $\kappa = 2, 6, 10, \dots, 58$) is not significant compared with that of NP, and the jumping-order behaviour of these modes gradually weakens with increasing inflow angle.

4.2.2. Eigenvalues and spectra of DMD modes

The importance of each DMD mode is quantified by the dynamic factor $d_i = |s_i| \times |\lambda_i|^m$ proposed by Statnikov, Meinke & Schröder (2017), where superscript ‘ m ’ is the snapshot number, and s_i and λ_i are the amplitude and eigenvalue, respectively, of the DMD mode, as shown in (A10). In addition to amplitude $|s_i|$, a decay term $|\lambda_i|^m$ in the dynamic factor can identify transient or spurious modes with high amplitudes but high decay rates. The dynamic factor of each mode is normalized by the maximum dynamic factor in each case. Similar to the sparsity-promoting (SP) method (Jovanović, Schmid & Nichols 2014), the dynamic factor method was demonstrated to be effective for identifying the dominant modes in the rotor wake (Magionesi *et al.* 2018; Shi *et al.* 2022).

According to the DMD spectra in figure 15, the DMD modes can be classified into four clusters (the modal clusters are independent of the group classification of destabilization mechanisms in § 3.1): (i) $\kappa = [4: 4: 60]$; (ii) $\kappa = [2: 4: 58]$; (iii) $\kappa = [1: 2: 59]$; and (iv) among the leading 25 modes with the highest dynamic factors, with the exception

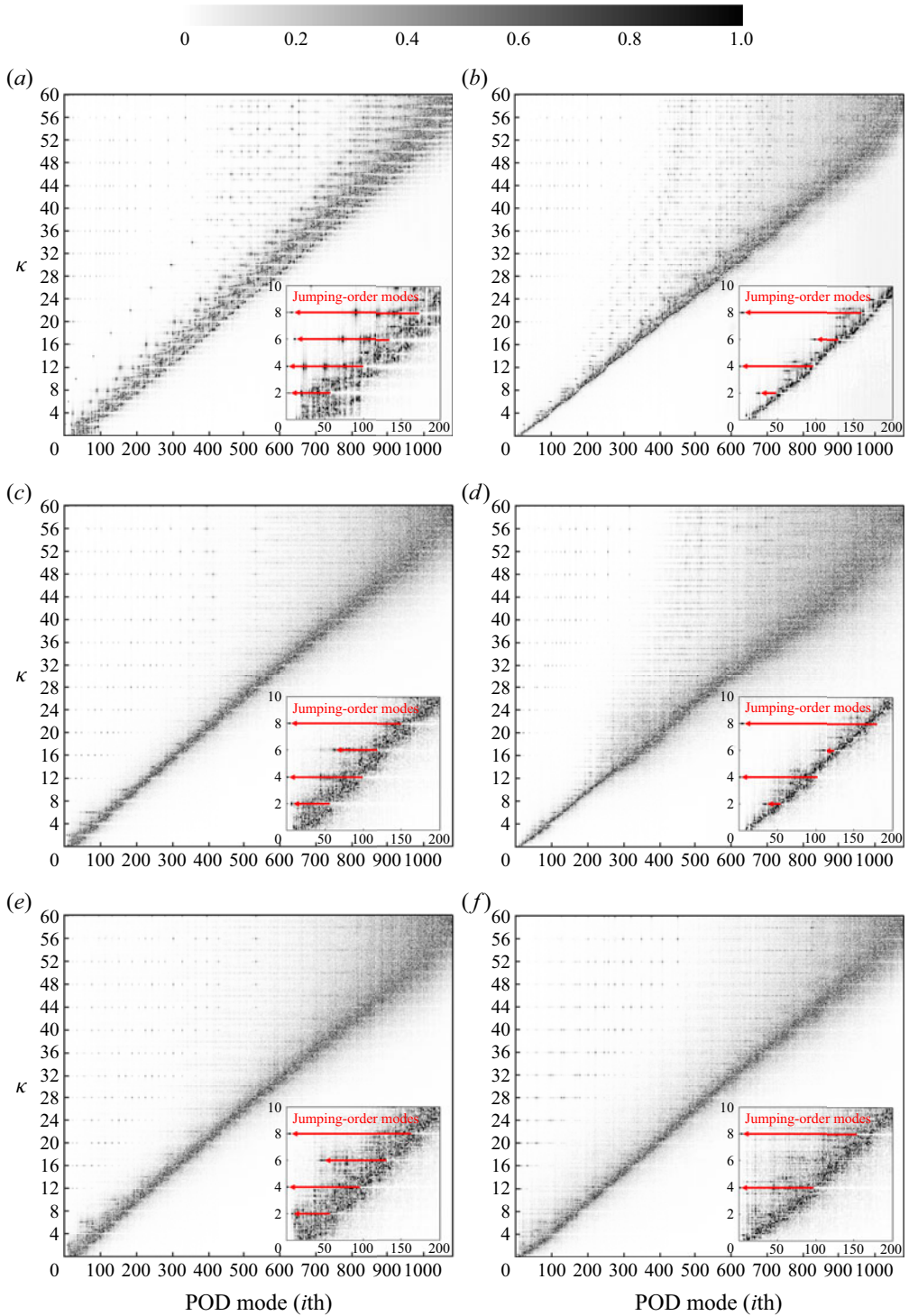


Figure 14. Spectral peak distribution of POD modes for the NP at (a) $\alpha = 0^\circ$, (c) 45° and (e) 60° and the DP at (b) $\alpha = 0^\circ$, (d) 45° and (f) 60° . The PSD is normalized by the spectral peak value of each mode.

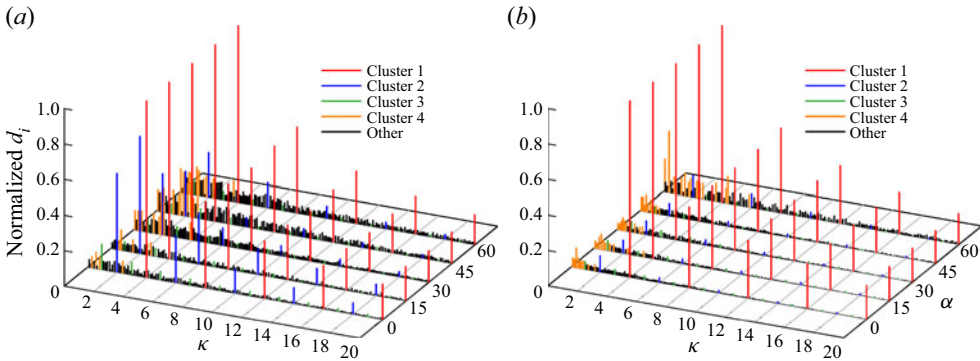


Figure 15. Spectral distribution of DMD modes for the (a) NP cases and (b) DP cases. The DMD spectra are normalized by the maximum dynamic factor in each case.

of the modes in the first three clusters, the remaining modes are classified as Cluster 4. Magionesi *et al.* (2018) and Shi *et al.* (2022) classified similar modal clusters for the propeller wake based on SP-DMD and the reduced-order reconstruction method, respectively. Analogously, the cluster classification of DMD modes is also effective for POD modes according to the modal jumping-order behaviour in figure 14.

In Clusters 1–3, the dynamic factor (importance) in each cluster decreases with increasing modal frequency. Cluster 1 is important for both the NP wake and DP wake, and its importance is not influenced by the inflow angle α . The importance of Cluster 2 is higher in the NP wake than in the DP wake, and the importance of Cluster 2 in the NP wake decreases with increasing α . Cluster 3 is important only for the NP at $\alpha = 0^\circ$. The number of modes in Cluster 4 reflects the degree of wake instability. With the aggravation of wake instability, some high-frequency modes in Clusters 1–3 become insignificant and the number of modes in Cluster 4 increases.

Figure 16 shows the eigenvalue distribution of DMD modes for the NP and DP at $\alpha = 60^\circ$. Assuming that a DMD mode has a complex eigenvalue of $\lambda_i = a + ib$, the modal frequency and growth/decay rate are denoted as

$$g_i + i2\pi f_i = \ln(\lambda_i)/\Delta t_s = \ln(a + ib)/\Delta t_s = \ln(a^2 + b^2)/(2\Delta t_s) + i \tan^{-1}(b/a)/\Delta t_s, \tag{4.1}$$

as shown in (A6) and (A7). Consequently, pairs of eigenvalues with the same frequency are symmetric with respect to the real axis, and the modal frequency increases with increasing argument. The growth/decay rate of modes is represented by the absolute value of their eigenvalues. Even for the severely destabilized wakes of the NP and DP at $\alpha = 60^\circ$, the eigenvalues are tightly clustered along the unit circle except for a few outliers (i.e. transient or spurious modes). Therefore, most modes have nearly zero growth/decay rates, indicating that the modes converge (Aaron, Schmidt & Colonius 2018).

4.3. Modal results

Based on the modal classification in § 4.2.2, the spatial and temporal characteristics of the dominant modes in the four clusters are discussed in this section. Since the mean flow is not subtracted from the datasets for DMD, DMD identifies the mean flow modes as the $\kappa = 0$ modes in figure 16. The mean flow modes present only a mean vorticity distribution but have no contribution to the turbulence effects in the wake. In addition, according to

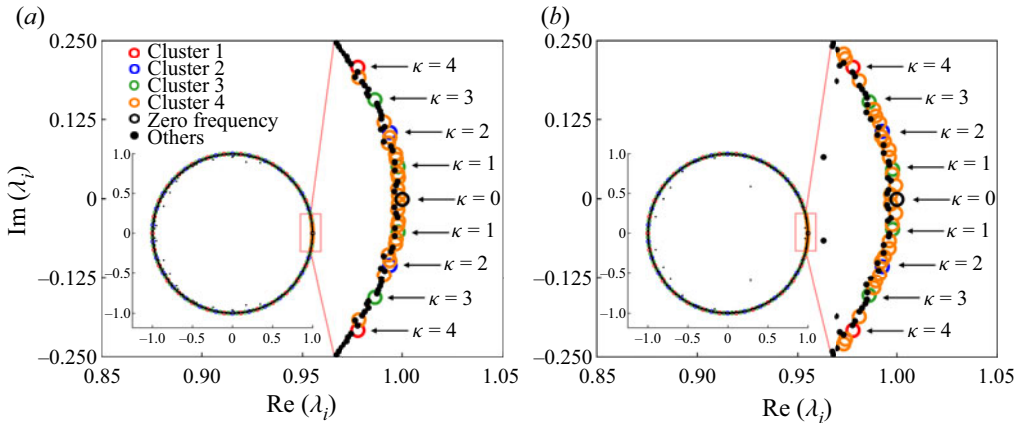


Figure 16. Eigenvalue distribution of DMD modes for the (a) NP at $\alpha = 60^\circ$ and the (b) DP at $\alpha = 60^\circ$. The eigenvalues of low-frequency modes with $\kappa \leq 4$ are shown enlarged on the right.

previous reduced-order reconstruction results (Shi *et al.* 2022), the spatial scale of modes decreases with increasing modal frequency. The low-frequency modes in each cluster play a dominant role in reproducing large-scale flow structures, while the contribution of high-frequency modes to the wake dynamics is small. Therefore, both zero-frequency and high-frequency modes are not discussed in this section.

4.3.1. $\kappa = 4$

Figures 17 and 18 demonstrate the first POD mode and the $\kappa = 4$ DMD modes, respectively. The iso-surface value and the legend of contours are not detailed in the modal visualization as the POD and DMD modes represent only the flow morphologies in space, and the iso-surface values and the minimum and maximum values of the contours have no physical relevance (Hamilton, Tutkun & Cal 2015; Noack *et al.* 2016; Magionesi *et al.* 2018). The combination of the spatial modes with the time coefficients ((A2) for POD and (A9) for DMD) is applied to reconstruct the wake field (Shi *et al.* 2022).

The $\kappa = 4$ DMD modes in figure 18 are correlated to the interaction between the trailing edge vortices and the helices. Compared with the spatiotemporally coupled vorticity field in figure 5, the modal decomposition methods better identify the individual helices in the outer slipstream, especially for the DP wakes in an oblique inflow where the helices are coupled with the secondary vortices into a vortex tube. Furthermore, the occurrence of helix short-wave instability at the frequency of $\kappa = 4$ indicates that the short-wave instability is caused by the torsion exerted on the helices by the trailing edge vortices during their interaction, as reported by Ricca (1994), Ahmed *et al.* (2020), Gong *et al.* (2021) and Shi *et al.* (2022).

Another destabilization mechanism characterized by $\kappa = 4$ is the merging between the helices and the ends of the trailing edge vortices, as marked by rectangular boxes in figure 18. Since the trailing edge vortices are susceptible to viscous dissipation, they gradually break down during downstream convection, and subsequently, the broken trailing edge vortices merge with the helices under the induction of the helices.

Moreover, in the windward region of the DP at $\alpha = 60^\circ$, the vortex shedding from the windward nozzle leading edge and the time-dependent shed vortices perturb the vorticity distribution on the nozzle inner sidewall (figures 5 and 6). The vorticity on the nozzle inner sidewall is involved in the formation of the helices, while the unused vorticity is

Effects of a nozzle on the propeller wake

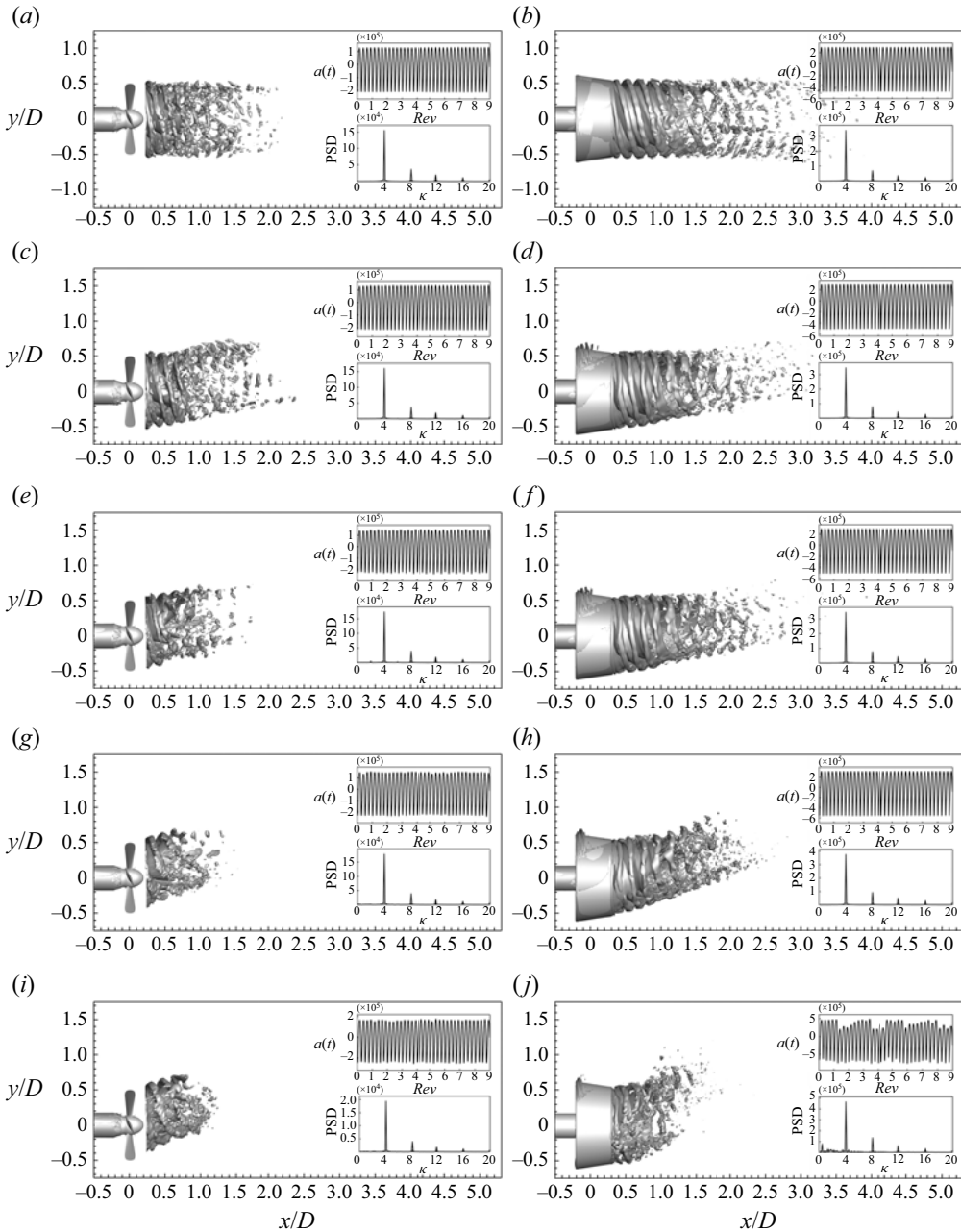


Figure 17. Iso-surfaces (left) and contours (right) of the first POD modes for the NP at (a) $\alpha = 0^\circ$, (c) 15° , (e) 30° , (g) 45° and (i) 60° , and the DP at (b) $\alpha = 0^\circ$, (d) 15° , (f) 30° , (h) 45° and (j) 60° .

induced by the trailing edge vortices to form the strong trailing edge vortex ends near the helices. However, the strong trailing edge vortex ends are easily separated from the trailing edge vortices and form additional vortex structures that are independent of the helices and the trailing edge vortex main bodies, as shown in [figure 18\(j\)](#). Note that the trailing edge vortex ends are not separated from the trailing edge vortices in the spatiotemporally

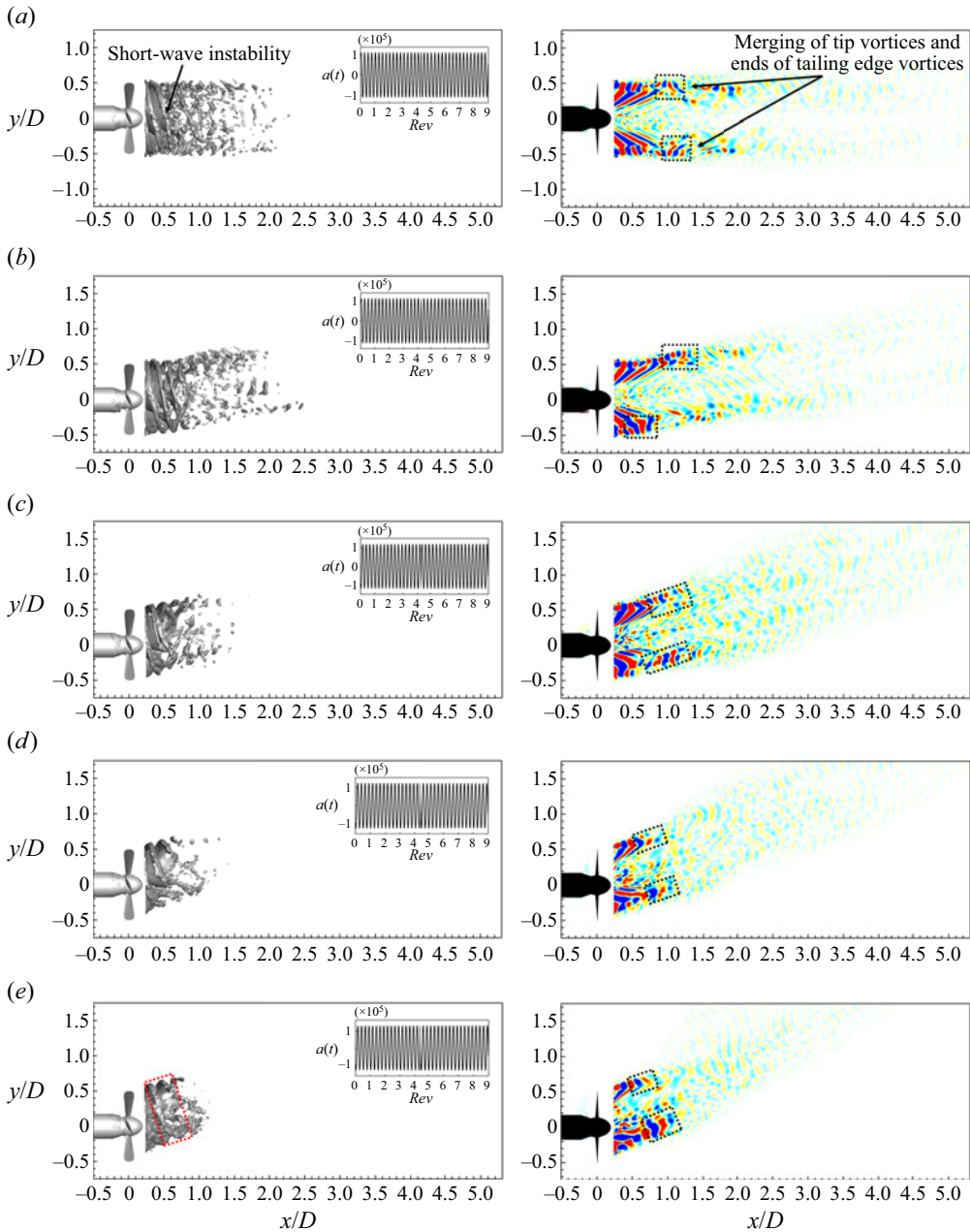


Figure 18. Iso-surfaces (left) and contours (right) of the $\kappa = 4$ DMD modes for the NP at (a) $\alpha = 0^\circ$, (b) 15° , (c) 30° , (d) 45° and (e) 60° .

coupled vorticity field in figure 5(j) because the disconnected part of the trailing edge vortices are characterized by other frequencies and are invisible in the $\kappa = 4$ mode.

In figures 17 and 18, the spatial morphologies of the $\kappa = 4$ DMD modes are similar to those of the first POD modes. DMD modes have a single-frequency characteristic, but the first POD modes are characterized by multiple frequencies, with a dominant spectral peak at $\kappa = 4$, a second lower peak at $\kappa = 8$, a third lower peak at $\kappa = 12$, etc. (figure 17).

Effects of a nozzle on the propeller wake

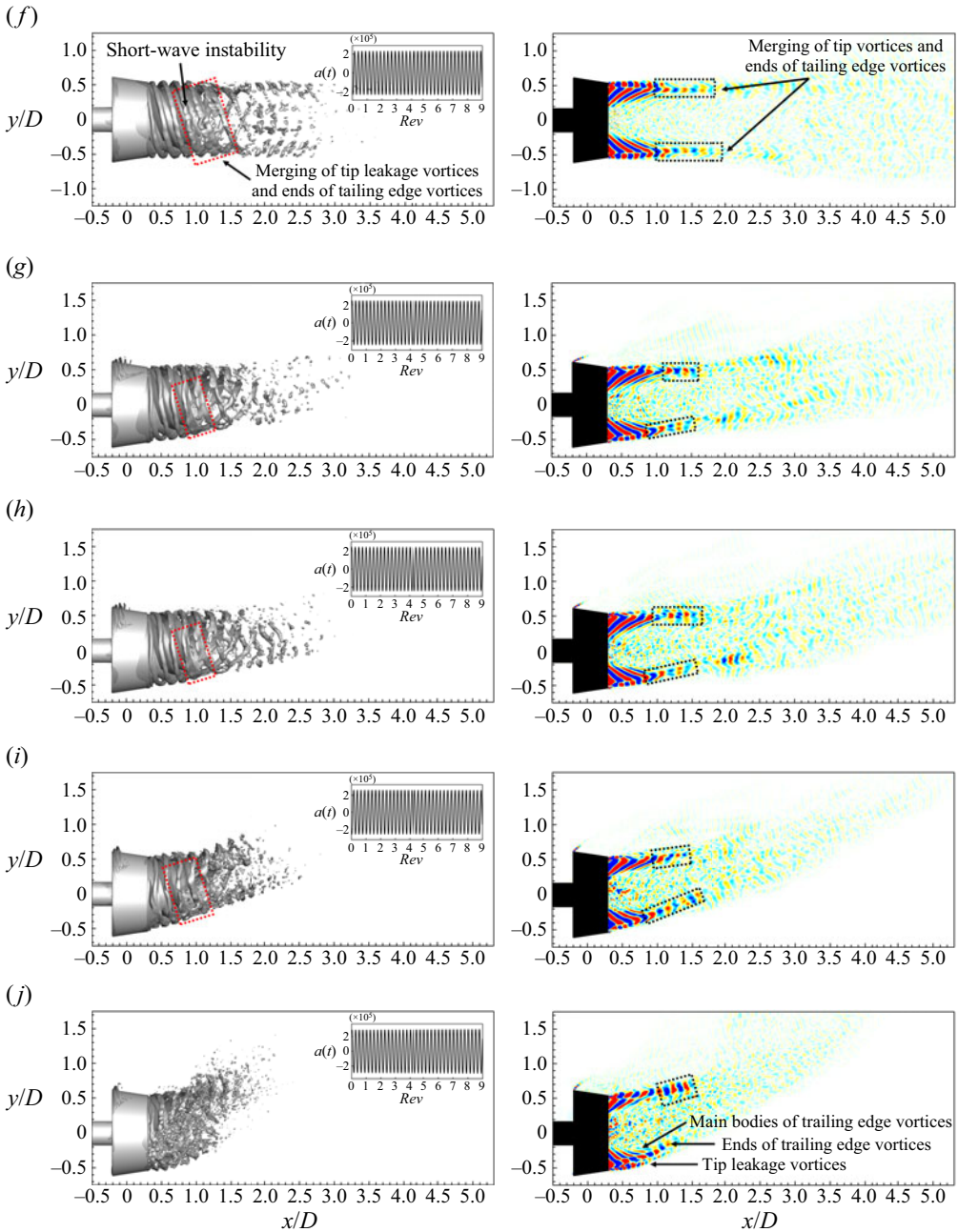


Figure 18. (Continued). Iso-surfaces (left) and contours (right) of the $\kappa = 4$ DMD modes for the DP at (f) $\alpha = 0^\circ$, (g) 15° , (h) 30° , (i) 45° and (j) 60° .

To investigate the temporal characteristics of the POD and DMD modes, [figure 19](#) illustrates the time coefficients of the first and second POD modes and the real and imaginary parts of the $\kappa = 4$ DMD modes, and the Lissajous figure is further applied to depict the phase portraits and to evaluate the phase difference between the time coefficients of the mode pairs, as shown in [figure 20](#). The circular trajectories of the real and imaginary

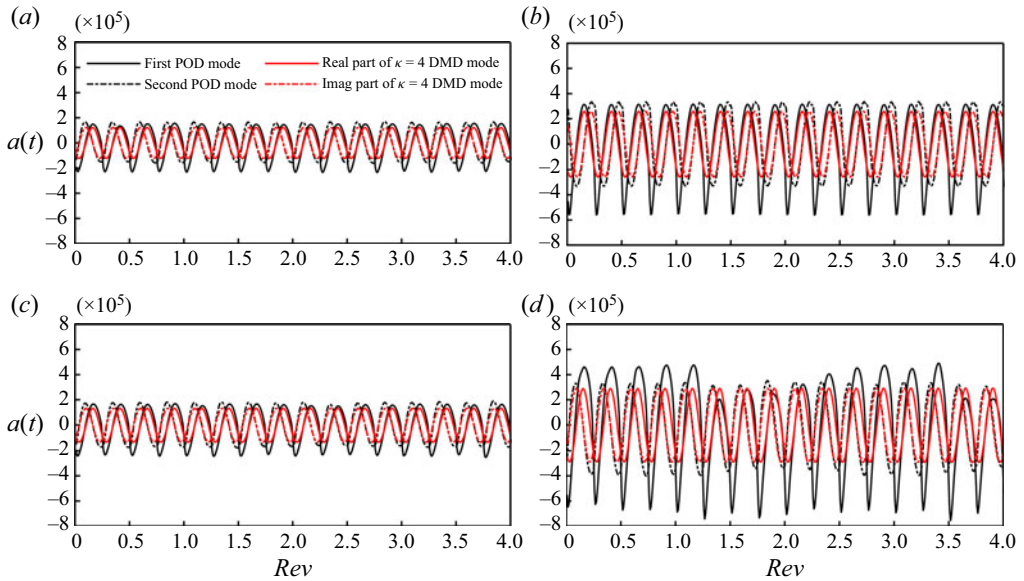


Figure 19. Time coefficients of the first and second POD modes and the real and imaginary parts of the $\kappa = 4$ DMD modes for the NP at (a) $\alpha = 45^\circ$ and (c) 60° , and the DP at (b) $\alpha = 45^\circ$ and (d) 60° .

parts of the $\kappa = 4$ DMD modes imply that their time coefficients follow a sinusoidal function but with a 90-degree phase shift. However, for the first and second POD modes, their multifrequency characteristics (figure 17) and amplitude fluctuations (figure 19) result in irregular circular trajectories in figure 20.

For periodic flow phenomena, the real and imaginary parts of a complex DMD mode ϕ_i can be approximately represented by the pair of same-frequency POD modes $\psi_j + i\psi_{j+1}$ (Schmid, Violato & Scarano 2012). Even if the POD mode pair has multiple spectral peaks, the two POD modes have similar spatial morphologies to the corresponding complex DMD mode if the POD modes have the same dominant spectral peak as the single-frequency DMD mode (Shi *et al.* 2022). The frequency matching holds for the $\kappa = 4$ DMD modes and the first and second POD modes in the present work.

For both POD mode and DMD mode, their spatial scale decreases with increasing frequency. According to Magionesi *et al.* (2018) and Shi *et al.* (2022), the $\kappa = 8$ DMD mode (or the POD mode with a dominant spectral peak at $\kappa = 8$) has the same spatial features as the $\kappa = 4$ DMD mode (or the POD mode with a dominant spectral peak at $\kappa = 4$), but the spatial scale of the former high-frequency mode is half that of the latter low-frequency mode. Furthermore, based on the DMD reconstruction, Shi *et al.* (2022) reported that the large-scale mode characterized by $\kappa = 4$ is dominant in the modal cluster $\kappa = [4: 4: 60]$, and the remaining $\kappa = [8: 4: 60]$ modes mainly add small-scale flow features. Therefore, high-frequency modes with $\kappa > 4$ are not the focus of this work and are not shown here for the sake of conciseness.

Since the spatial morphologies of DMD modes are similar to those of the corresponding POD modes and the single-frequency characteristic of DMD modes is convenient for seeking the physical relevance of the modes, the modal analysis in the remaining discussion is mainly based on the DMD modes.

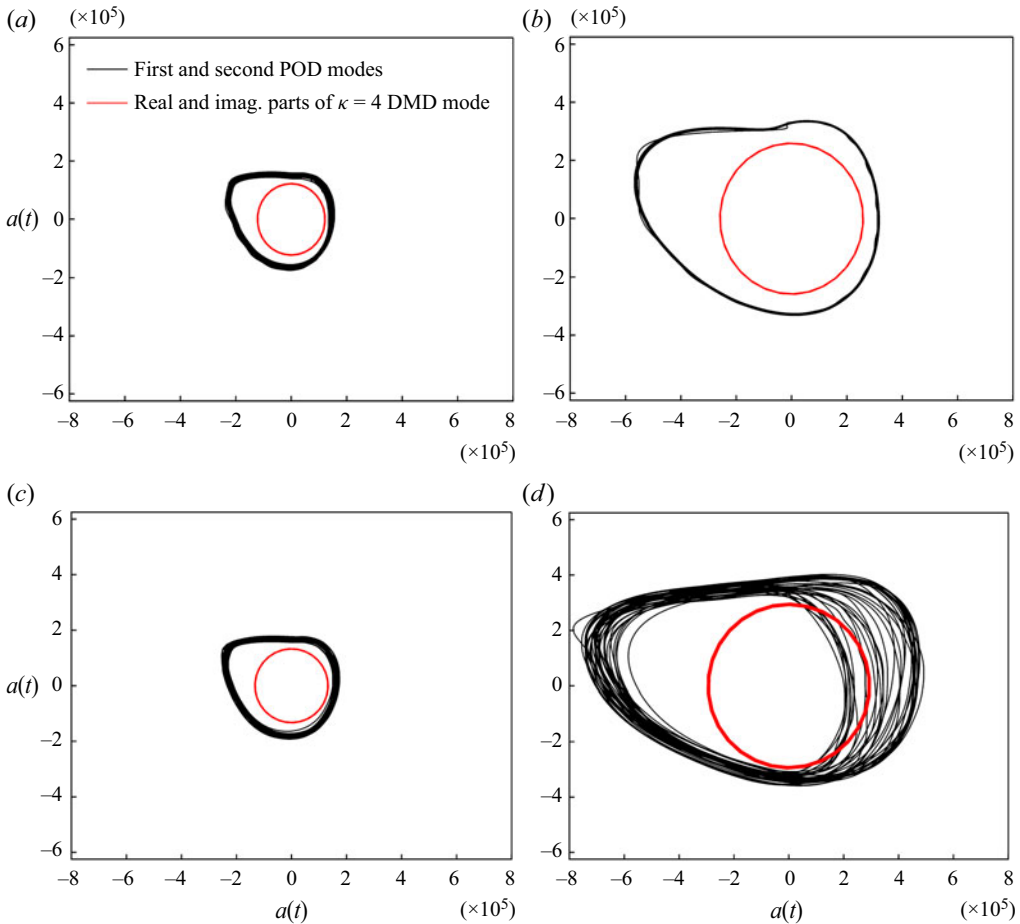


Figure 20. Phase portraits of the first and second POD modes and the real and imaginary (imag.) parts of the $\kappa = 4$ DMD modes for the NP at (a) $\alpha = 45^\circ$ and (c) 60° , and the DP at (b) $\alpha = 45^\circ$ and (d) 60° .

4.3.2. $\kappa = 2$

The $\kappa = 2$ DMD modes shown in figure 21 are mainly associated with the merging of adjacent helices, especially for the NP at $\alpha = 0^\circ, 15^\circ, 30^\circ, 45^\circ, 60^\circ$ and the DP at $\alpha = 0^\circ$ (i.e. Group 1; details in § 3.1), where the helix pairing phenomenon is visible in the outer slipstream in figures 4 and 5. However, for the DP at $\alpha = 15^\circ, 30^\circ, 45^\circ, 60^\circ$ (i.e. Group 2), a vortex tube is formed in the outer slipstream, followed by the rolling-up of the vortex tube in the windward region (figures 4 and 5). Therefore, the pairing between adjacent helices is invisible in the spatiotemporally coupled flow field of Group 2.

In general, if the rolled-up vortex tube does not contain any helices, its generation should be a stochastic process and its characteristic frequency should not be $\kappa = 2$. However, the helix pairing characterized by $\kappa = 2$ occurs in the windward region of Group 2 (figure 21g,h,i,j), implying that the rolled-up vortex tube contains the pairing of two adjacent helices, as depicted in figure 6. However, in the leeward region of Group 2, the vortex shedding from the leeward nozzle leading edge interacts so strongly with the helices that the helices break down before they pair up, and consequently, the helix pairing is insignificant in this region in figure 21(g,h,i,j).

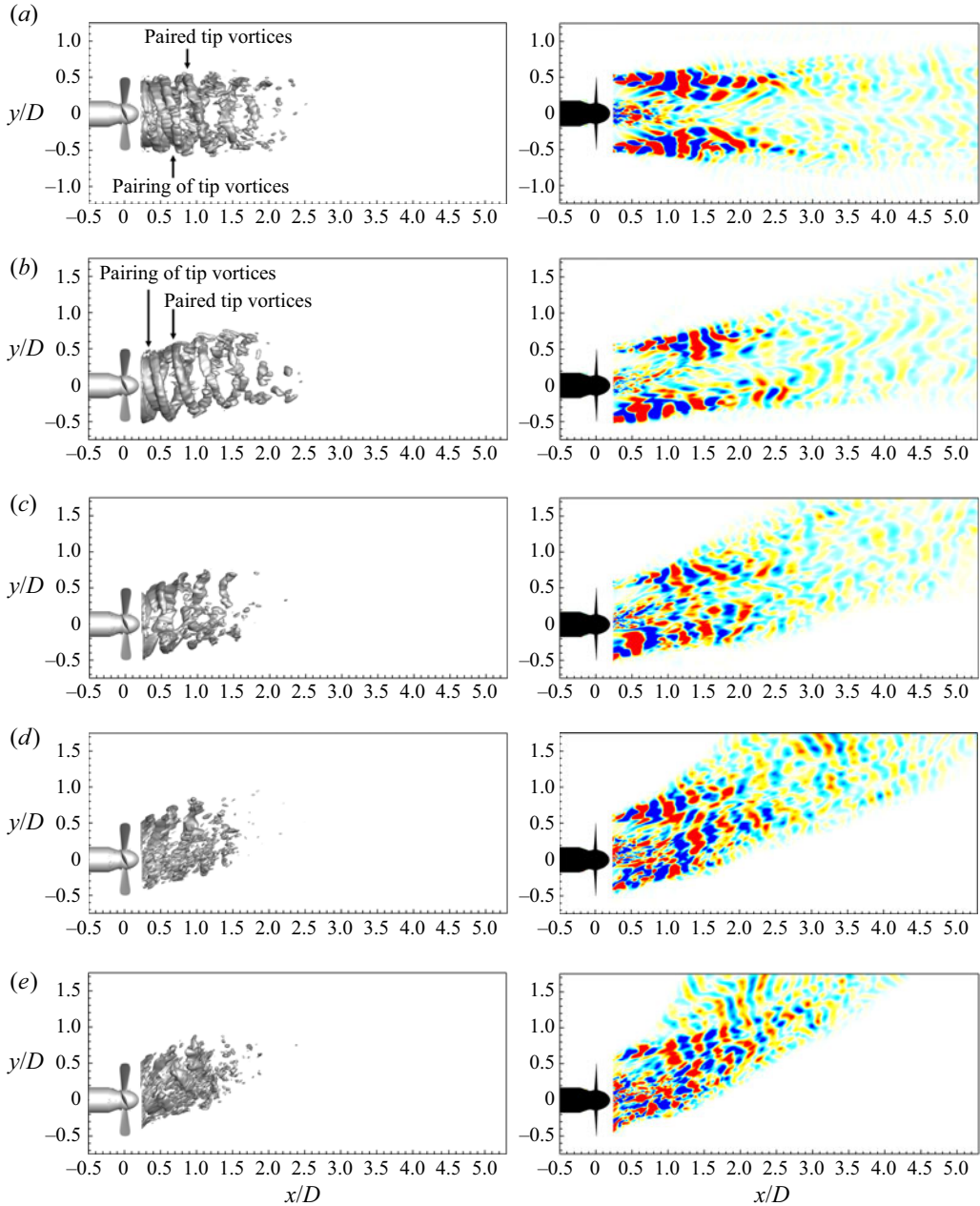


Figure 21. Iso-surfaces (left) and contours (right) of the $\kappa = 2$ DMD modes for the NP at (a) $\alpha = 0^\circ$, (b) 15° , (c) 30° , (d) 45° and (e) 60° .

4.3.3. $\kappa = 1$

According to the DMD spectra in figure 15, the $\kappa = 1$ mode is important only for the NP at $\alpha = 0^\circ$. The $\kappa = 1$ mode shown in figure 22 is associated with the hub vortex instability and the expansion of merged helices in the radial direction. The merged helices expand in the radial direction at approximately $x/D = 1.5$, immediately after the completion of the helix pairing characterized by $\kappa = 2$ in figure 21(a). As highlighted by Felli *et al.* (2011),

Effects of a nozzle on the propeller wake

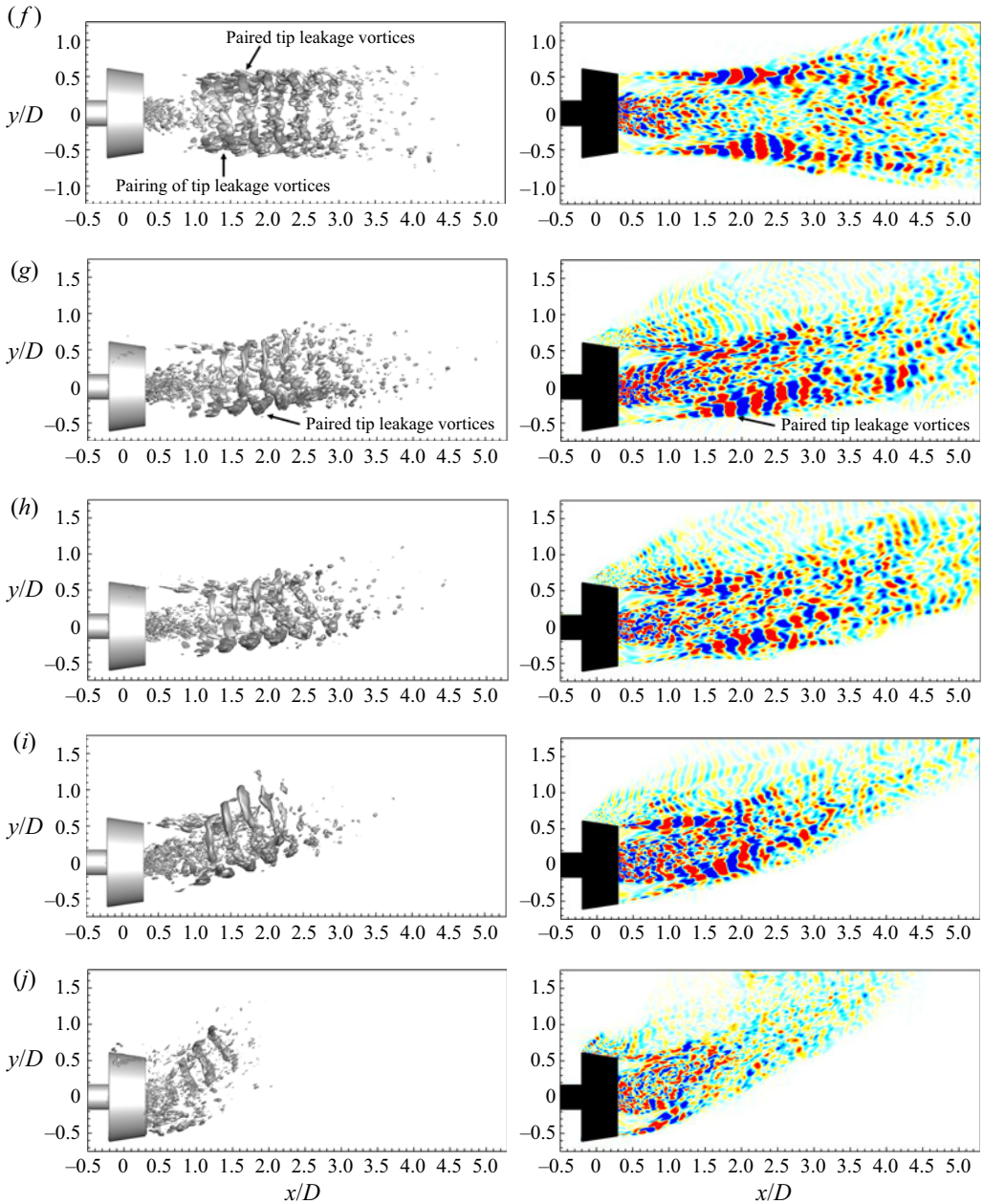


Figure 21. (Continued). Iso-surfaces (left) and contours (right) of the $\kappa = 2$ DMD modes for the DP at (f) $\alpha = 0^\circ$, (g) 15° , (h) 30° , (i) 45° and (j) 60° .

Kumar & Mahesh (2017) and Ahmed *et al.* (2020), the trailing edge vortices have a crucial role in maintaining the relative position between the helices and the hub vortex. After the trailing edge vortices are fully broken down (at approximately $x/D = 1.5$, as shown in figure 5a), the merged helices in the outer slipstream are no longer induced by the trailing edge vortices and expand in the radial direction with great rotational inertia.

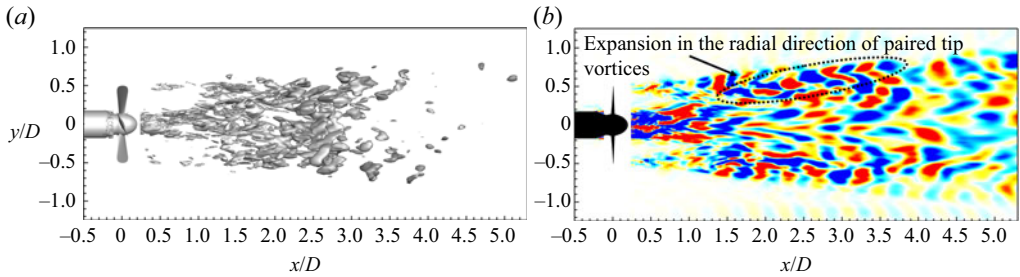


Figure 22. Iso-surfaces (a) and contours (b) of the $\kappa = 1$ DMD mode for the NP at $\alpha = 0^\circ$.

Similarly, for the E779A propeller in an axisymmetric flow with $\alpha = 0^\circ$, Magionesi *et al.* (2018) and Wang *et al.* (2022) related the $\kappa = 1$ modes to the precession motion of the propeller outer slipstream and the long-wave instability of the hub vortex. In contrast to the unstable hub vortex in this work, the hub vortex in their work is stable near the propeller and begins to distort at approximately two diameters downstream of the propeller disk.

4.3.4. $\kappa < 1$

The modes in the range of $0 < \kappa < 1$ are mainly correlated with the shear motion and rotational effects in the wake. Among these modes, the modes near zero frequency are dominated by the shear effect. From the DMD spectra in figure 15, the modes near zero frequency are insignificant for the NP at $\alpha = 0^\circ$ and 15° , and thus, figure 23 demonstrates the modes near $\kappa = 0.1$ in the other eight cases.

For the NP, the modes near zero frequency are characterized by large-scale vortex clumps in the outer slipstream and shear deformation of the hub vortex. In figure 9(c), the angle deviation between the inflow angle and the deflection angle of the nominal wake centre (representative of the main flow) increases with increasing inflow angle. Consequently, the velocity component in the main flow direction decreases with increasing inflow angle. The shear effect becomes increasingly intense with increasing inflow angle, and the shear modes are prominent for the NP only at large inflow angles ($\alpha \geq 30^\circ$).

For the DP, the nozzle exerts a strong shear on the helixes, and the shear modes are strong at any inflow angle. Three-layer vortex surfaces are observed in the DP wake in figure 23(d–h). For the DP wake in an axisymmetric flow and the DP windward wake in an oblique flow, the outermost shear layer vortex surfaces are related to the shear exerted by the nozzle and the free stream on the helixes. In contrast, in the leeward region of the DP in an oblique flow, the outermost vortex surfaces are generated by the interaction between the helixes and the low-frequency vortex shedding from the leeward nozzle leading edge.

In the windward and leeward regions of the DP at any inflow angle (including $\alpha = 0^\circ$), the middle and innermost vortex surfaces are associated with the convection of the trailing edge vortices with the outer helixes and the inner turbulence. Eventually, the middle and innermost vortex surfaces tend to merge after the breakdown of the trailing edge vortices (figure 23d–h).

With increasing κ , the shear effect in the wake weakens, but the rotational effect is enhanced. Figure 24 shows the dominant modes with the highest dynamic factor in the range of $0 < \kappa < 1$, with the exception of the modes near $\kappa = 0.1$. Compared with the shear modes near zero frequency in figure 23, the modes with an increased frequency have a more pronounced helical morphology in the outer slipstream. According to previous reduced-order reconstruction results (Shi *et al.* 2022), the far-wake meandering

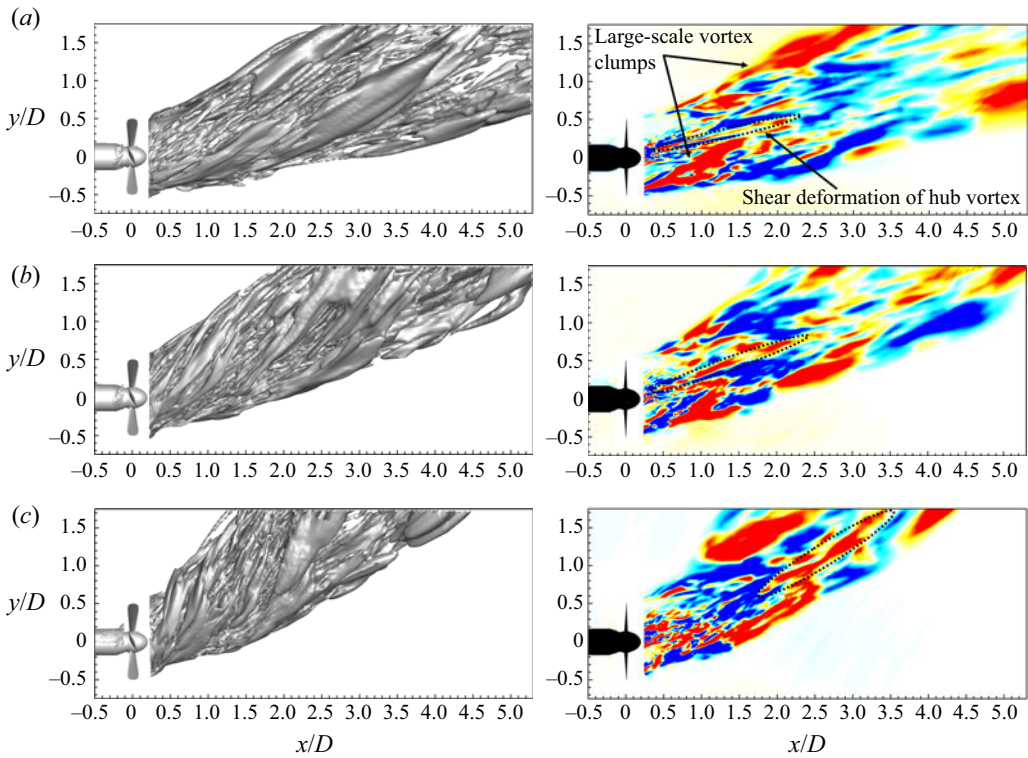


Figure 23. Iso-surfaces (left) and contours (right) of the DMD modes near zero frequency for the NP at (a) $\alpha = 0^\circ$, (b) 15° and (c) 30° . (a) NP $\alpha = 30^\circ$, $\kappa = 0.11$; (b) NP $\alpha = 45^\circ$, $\kappa = 0.13$ and (c) NP $\alpha = 60^\circ$, $\kappa = 0.12$.

phenomenon is dominated by low-frequency modes with large-scale helical vortices in the outer slipstream. Thus, the modes in figure 24 are associated with wake meandering. Some previous literature reported that the long-wave instability of the hub vortex drives wake meandering as the large-scale helical vortices in the outer slipstream propagate downstream at the same frequency as the hub vortex distortions (Felli *et al.* 2011; Iungo *et al.* 2013; Howard *et al.* 2015; Foti *et al.* 2018a; Magionesi *et al.* 2018). Similarly, the same-frequency oscillations of the hub vortex with the outer helical vortices are also identified in the NP wake (figure 24a–e).

However, Kang *et al.* (2014) and Yang & Sotiropoulos (2019) reported that hub vortex distortion is not the trigger for wake meandering, but it might energize large-scale meandering motions. Furthermore, Mao & Sørensen (2018) and Foti *et al.* (2018a) reproduced wake meandering without modelling a hub vortex and stated that the shear from the free stream induces the meandering motion. In the current work, wake meandering is present in the DP wake, where the hub vortex is broken down into chaotic turbulence. Therefore, the meandering motion seems to be directly induced by the large-scale helical vortices in the outer slipstream but not driven by the hub vortex.

The helical vortices are initially generated by the unstable vortices at the outer boundary of the slipstream via shear. After the trailing edge vortices break down, the vortex structures in the inner slipstream progressively expand outwards and eventually merge with the outer helical vortices. Under strong shear and large rotational inertia, the precession motion of merged large-scale helical vortices in the outer slipstream dominates the wake meandering.

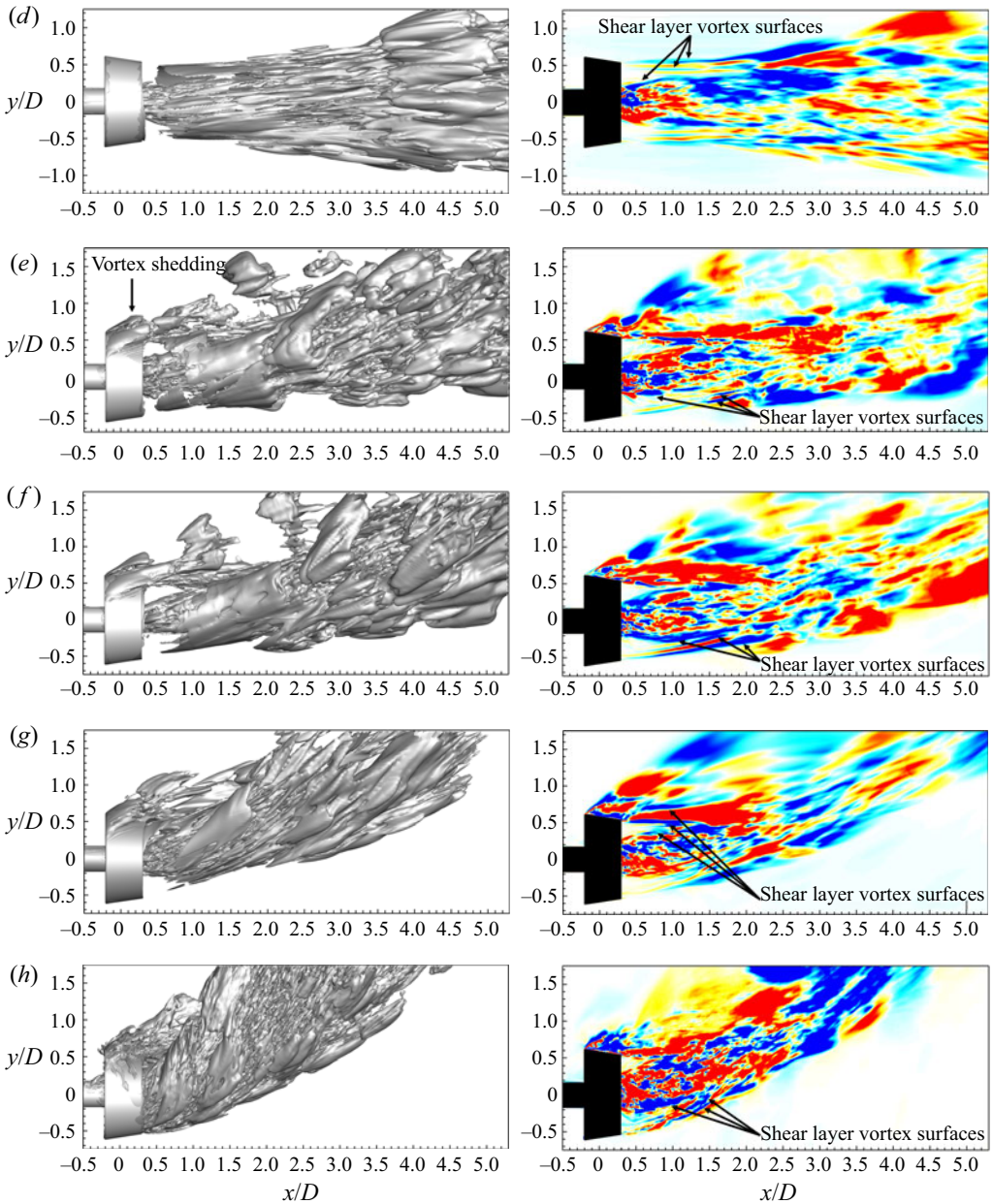


Figure 23. (Continued). Iso-surfaces (left) and contours (right) of the DMD modes near zero frequency for the DP at (d) $\alpha = 0^\circ$, (e) 15° , (f) 30° , (g) 45° and (h) 60° . (d) DP $\alpha = 0^\circ$, $\kappa = 0.13$; (e) DP $\alpha = 15^\circ$, $\kappa = 0.11$; (f) DP $\alpha = 30^\circ$, $\kappa = 0.09$; (g) DP $\alpha = 45^\circ$, $\kappa = 0.11$ and (h) DP $\alpha = 60^\circ$, $\kappa = 0.14$.

Generally, hub vortex distortions and far-wake meanderings are low-frequency, stochastic processes. The frequency of the dominant modes characterizing the two large-scale destabilization mechanisms is independent of the inflow angle, but these modes have a lower frequency for the DP than the NP at the same inflow angle, which is probably ascribable to the shear and deceleration effects of the nozzle on the propeller wake, as reported in [figure 11](#).

Effects of a nozzle on the propeller wake

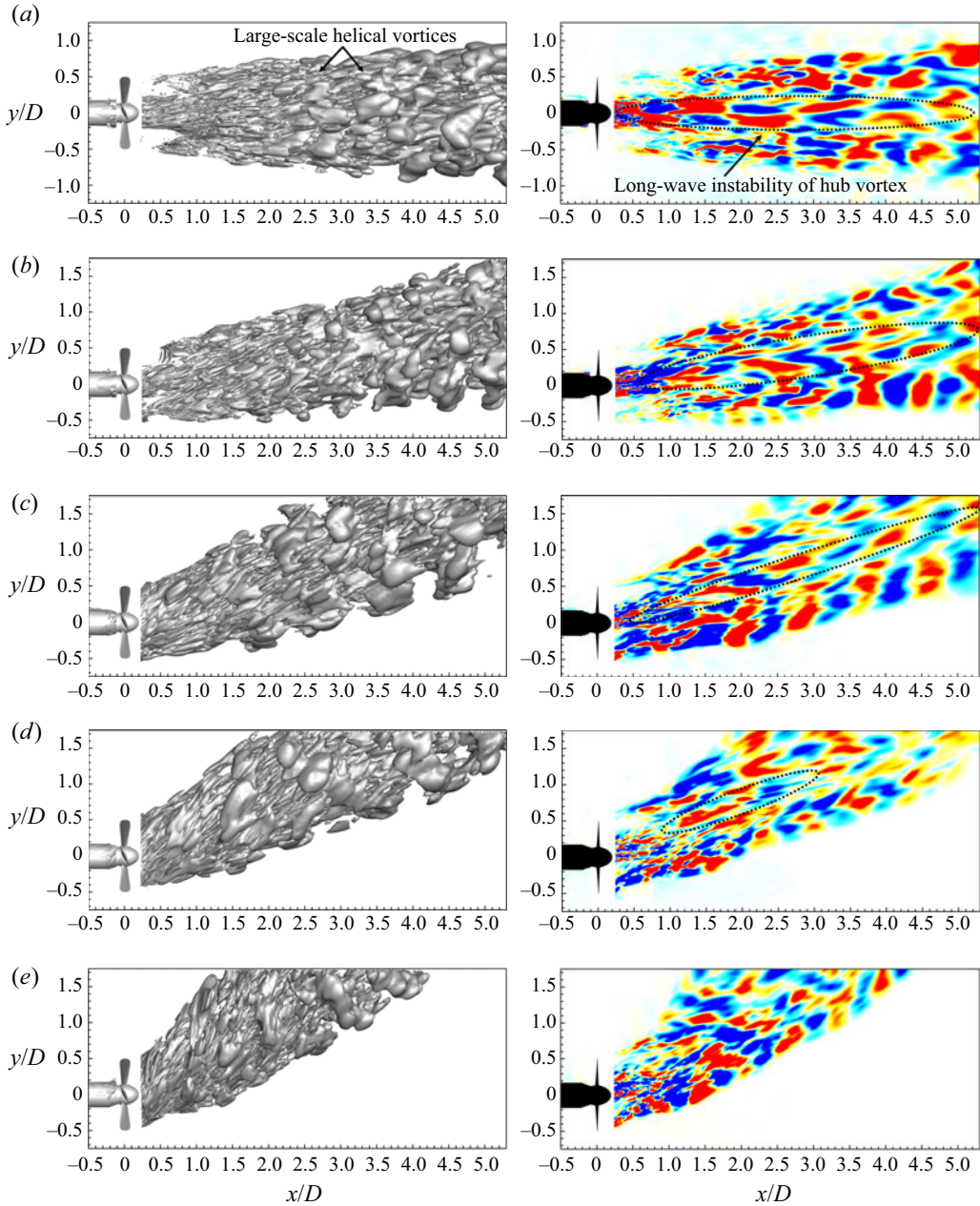


Figure 24. Iso-surfaces (left) and contours (right) of the wake meandering DMD modes for the NP at (a) $\alpha = 0^\circ$, (b) 15° , (c) 30° , (d) 45° and (e) 60° . (a) NP $\alpha = 0^\circ$, $\kappa = 0.60$; (b) NP $\alpha = 15^\circ$, $\kappa = 0.61$; (c) NP $\alpha = 30^\circ$, $\kappa = 0.57$; (d) NP $\alpha = 45^\circ$, $\kappa = 0.53$ and (e) NP $\alpha = 60^\circ$, $\kappa = 0.66$.

5. Conclusions

This study numerically investigates the destabilization mechanisms of the wake of a four-bladed (S5810 R) marine propeller with and without a (1393 type 19A) nozzle (NP and DP) in yawed conditions using a combination of the DDES turbulence model and the AMI mesh rotation method. The evolution characteristics of the NP and DP wakes under

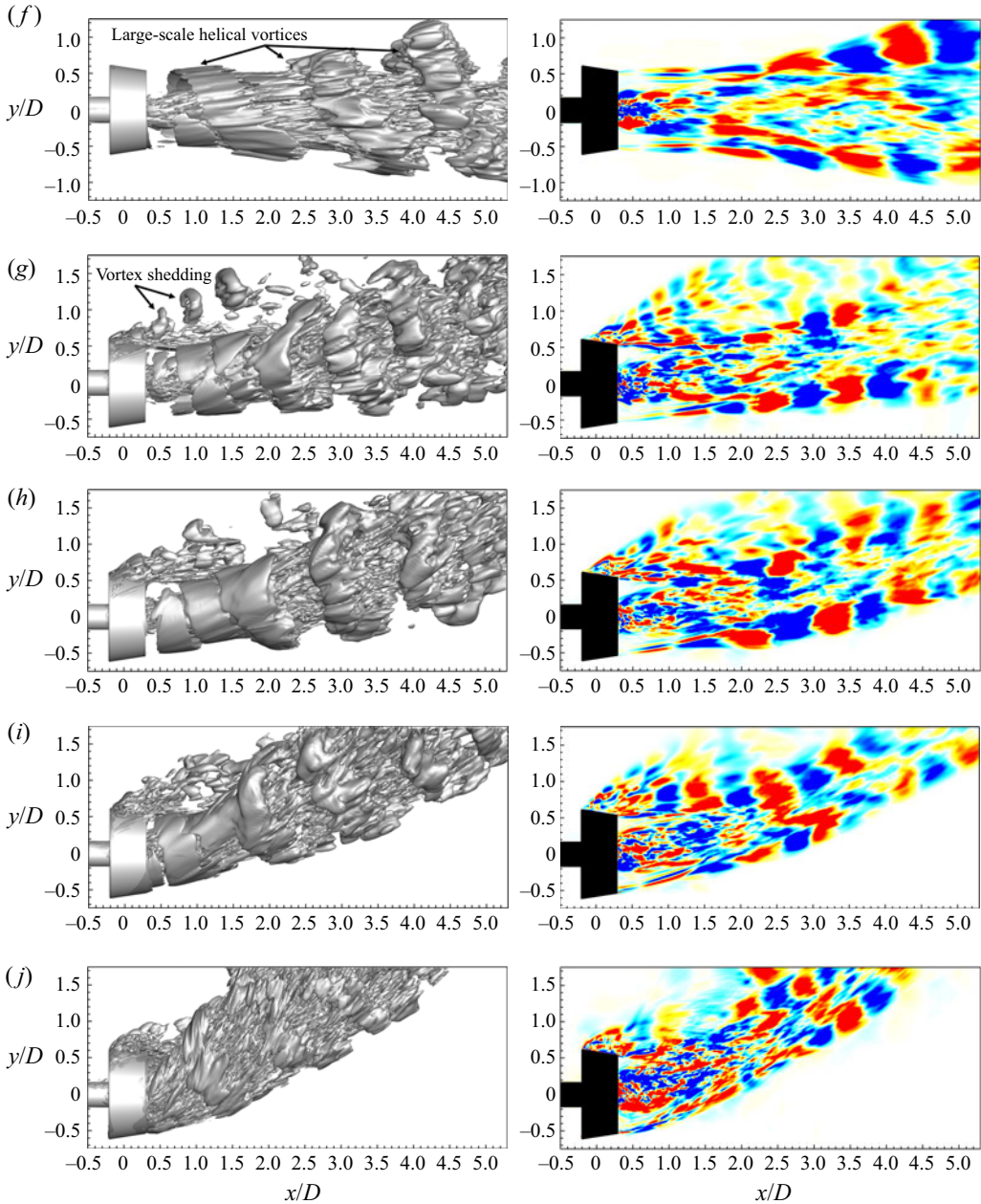


Figure 24. (Continued). Iso-surfaces (left) and contours (right) of the wake meandering DMD modes for the DP at (f) $\alpha = 0^\circ$, (g) 15° , (h) 30° , (i) 45° and (j) 60° . (f) DP $\alpha = 0^\circ$, $\kappa = 0.36$; (g) DP $\alpha = 15^\circ$, $\kappa = 0.52$; (h) DP $\alpha = 30^\circ$, $\kappa = 0.42$; (i) DP $\alpha = 45^\circ$, $\kappa = 0.44$ and (j) DP $\alpha = 60^\circ$, $\kappa = 0.42$.

the axisymmetric ($\alpha = 0^\circ$) and oblique flow conditions ($\alpha = 15^\circ, 30^\circ, 45^\circ$ and 60°) are systematically analysed at the moderate advance coefficient $J = 0.4$ using flow field and modal analysis.

Previous studies have highlighted the effect of the nozzle on the propeller wake in an axisymmetric flow, i.e. the nozzle decelerates the wake, weakens the vorticity intensity

Effects of a nozzle on the propeller wake

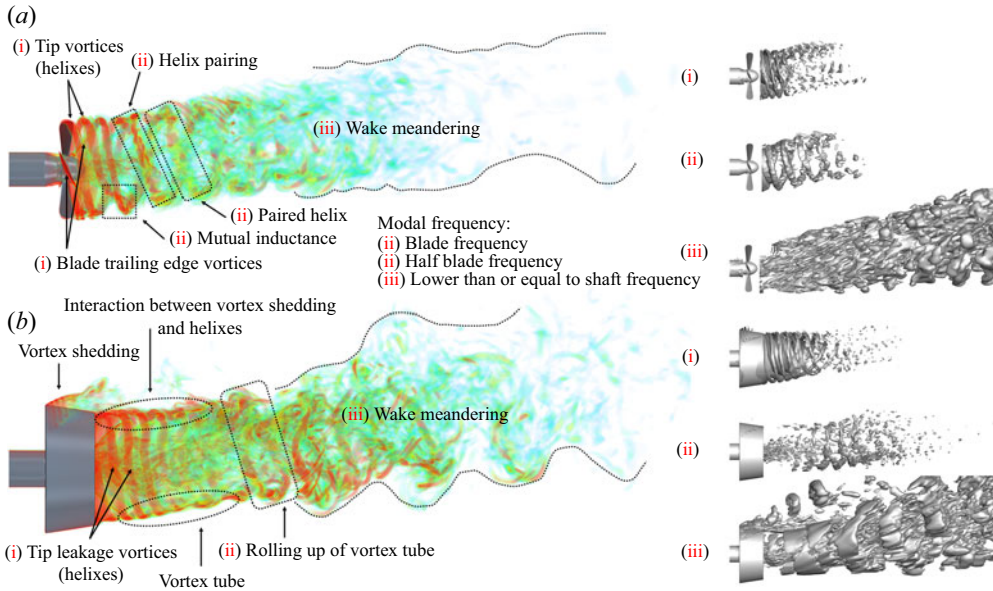


Figure 25. Vortex systems and dominant modes of the NP and DP wakes in an oblique flow. The serial numbers (i)–(iii) correspond to the modes characterized by the blade frequency, half blade frequency and a frequency lower than or equal to the shaft frequency.

of helices and breaks down the hub vortex into chaotic turbulence (Shi *et al.* 2022). As an extension work, the present study focuses mainly on the differences in the wake dynamic and destabilization mechanisms between the NP and the DP in an oblique flow, and in particular, the contribution of the nozzle to the wake deflection. The conclusions are summarized as follows.

- (i) The deflection angles of the helices in the outer slipstream obtained from the phased-averaged vorticity are employed to evaluate the wake deflection. In general, the outer slipstream in the windward region undergoes a more intense deflection than that in the leeward region, and the nozzle mitigates the wake deflection in the two regions.
- (ii) For the NP in an oblique flow, the helices are stronger on the windward side than on the leeward side, and the difference in the vortex core size of the helices between the two sides becomes more pronounced as the inflow angle increases. In contrast, the DP helices have similar vortex core sizes on the two sides and are independent of the inflow angle as their generation is dominated by the vortex redistribution on the nozzle inner sidewall.
- (iii) The dominant destabilization mechanisms in the outer slipstream of the NP in an oblique flow are the interaction between the blade trailing vortices and the helices in the near-wake region, the helix pairing in the transition region, and the stochastic wake meandering in the far-wake region, as shown in [figure 25\(a\)](#). The short-wake instability of the helices and the generation of secondary vortices are caused by the interaction between the downstream previously shed helices and the upstream trailing edge vortices. Generally, the NP wake in an oblique flow has similar destabilization mechanisms in the outer slipstream to the NP and DP wakes in axisymmetric flow. However, in the windward region of the NP wake in an oblique

flow, helices with large vortex core sizes accelerate the vortex interaction and wake destabilization.

- (iv) For the DP in an oblique flow, a tube-shaped wake envelope, as a consequence of the similar vorticity intensity between the helices and the secondary vortices wrapping around adjacent helices, is generated in the near-wake region, followed by the rolling-up of the vortex tube in the transition region (figure 25*b*). The vortex tube rolls up in the same direction as the helix rotation, and the rolling-up process involves the pairing of two adjacent helices. In addition, in the leeward region of the DP, the low-frequency vortex shedding from the leeward nozzle leading edge due to the inflow misalignment strongly interacts with the helices.

Modal decomposition methods, especially for DMD (detailed comparisons between POD and DMD are summarized by Shi *et al.* 2022), are powerful tools for visualizing modes with characteristic frequencies and for identifying the dominant destabilization mechanisms while avoiding the interference of disorder secondary turbulence.

From modal analysis, the spatial scale of flow phenomena decreases with increasing flow frequency. For both the NP and DP, even though disorder and small-scale vortices perturb the flow field, the dominant destabilization mechanisms in the near-wake, transition and far-wake regions are the interaction between the trailing edge vortices and the helices (characterized by the blade frequency, i.e. $\kappa = 4$), the helix pairing (characterized by the half blade frequency, i.e. $\kappa = 2$), and wake meandering (characterized by frequencies lower than or equal to the shaft frequency, i.e. $\kappa \leq 1$), respectively (figure 25). Although the wake meandering oscillates at the same frequency as the hub vortex long-wave distortions, the meandering is fundamentally dominated by the large-scale helical vortices driven by the propeller rotation and free stream shear. Furthermore, the occurrence frequency of wake meandering is independent of the inflow angle. Compared with the NP wake, the DP nozzle reduces the occurrence frequency of wake meandering and results in a more pronounced helical morphology of wake meandering.

Acknowledgements. The authors acknowledge Professor N. Wang for his valuable guidance and discussions. The authors are also grateful to Ir H. Cozijn and Dr Ir A. Koop from MARIN for providing the thruster geometry.

Funding. This work was supported by the National Natural Science Foundation of China (Q.Z., grant number 51979260), (H.D.S., grant numbers 52111530047 and 52071303); the National Key R & D Program of China (H.D.S., grant number 2018YFB1501900); the Shandong Provincial Natural Science Foundation (H.D.S., grant number ZR2021ZD23); the Shandong Provincial Key Research and Development Program (H.D.S., grant number 2019JZZY010902); the Joint Project of NSFC-SD (H.D.S., grant number U1906228); and the Taishan Scholars Program of Shandong Province (H.D.S., grant number ts20190914).

Declaration of interests. The authors report no conflict of interest.

Data availability statement. The data that support the findings of this study are available from the corresponding author upon reasonable request.

Author ORCIDs.

-  Tianyuan Wang <https://orcid.org/0000-0002-1802-0697>;
-  Hongda Shi <https://orcid.org/0000-0002-9386-6721>;
-  Ming Zhao <https://orcid.org/0000-0003-2000-2241>;
-  Qin Zhang <https://orcid.org/0000-0001-5010-9715>.

Author contributions. T.Y.W. performed the modal analysis and Q.Z. performed the simulations. All authors contributed equally to analysing data and reaching conclusions, and in writing the paper.

DP $\alpha = 0^\circ$	Rotor (million)	Stator (million)	Total (million)	Refinement ratio (%)
Coarse	0.69	5.11	5.79	
Medium	1.16	12.10	13.26	1.32
Fine	1.43	31.48	32.91	1.35

Table 4. Three grid densities for the DP at $\alpha = 0^\circ$.

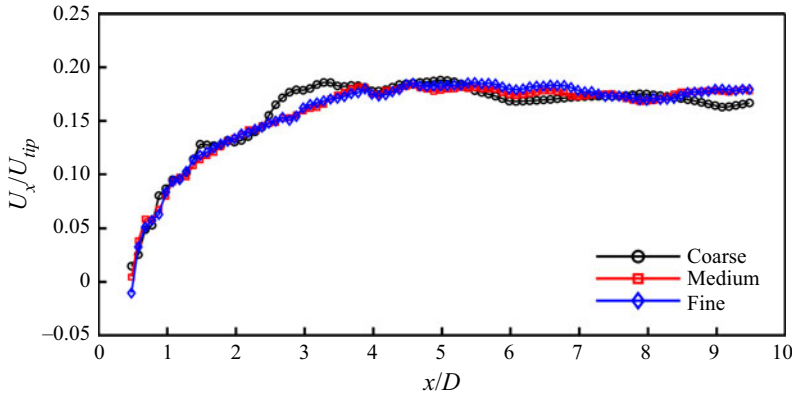


Figure 26. Comparison of time-averaged, x -direction velocity U_x along the line of $(y/D, z/D) = (0, 0)$ among the coarse, medium and fine meshes for the DP at $\alpha = 0^\circ$. The probes are inserted along the line of $(y/D, z/D) = (0, 0)$ from $x/D = 0.5$ to 9.5 with a spatial spacing of $0.1D$. The velocity is normalized by U_{tip} .

Appendix

A.1. Grid sensitivity study

Previous work (Zhang & Jaiman 2019) has compared the differences in the loadings and wake topology between the numerical simulations and the experimental measurements for the DP in zero inflow velocity, axisymmetric condition ($J = 0$ and $\alpha = 0^\circ$). With the same propeller and nozzle geometries and grid configuration, a grid sensitivity study of the DP with $J = 0.4$, $\alpha = 0^\circ$ case is further conducted in the present work. Detailed information about the adopted three grid densities, namely, coarse mesh (total 5.79×10^6), medium mesh (total 13.26×10^6) and fine mesh (total 32.91×10^6), is in table 4. Based on the three meshes, the time-averaged x -direction velocity U_x along the axis centreline ($y/D = 0$, $z/D = 0$) obtained by the transient simulation combining the DDES model and AMI method is shown in figure 26. The comparison of the velocity results indicates a slight difference between the medium mesh and fine mesh.

Apart from the velocity, the non-dimensional propeller thrust $K_{TPx} = T_{px}/(\rho n^2 D^4)$, nozzle thrust $K_{TNx} = T_{nx}/(\rho n^2 D^4)$ and propeller torque $K_{QPx} = Q_{px}/(\rho n^2 D^5)$ are also considered to evaluate the numerical uncertainty, where T_{px} , T_{nx} and Q_{px} are the propeller thrust, nozzle thrust and propeller torque, respectively, in the x direction. The grid convergence index (GCI) analysis described in Celik *et al.* (2008) is further performed on these quantities obtained by the transient DDES simulation, and the results of the DP case with $J = 0.4$ and $\alpha = 0^\circ$ are summarized in table 5. With the exception of the velocity at $x/D = 7$, the uncertainty of the fine mesh (GCI value) is lower than that of the medium mesh. Furthermore, the uncertainty in all quantities is lower than 6% for the fine mesh. Overall, the propeller and nozzle loads and wake velocity obtained from the medium mesh

DP $\alpha = 0^\circ$		Coarse	Medium	Fine	GCI _{Med} (%)	GCI _{Fine} (%)
	K_{TPx}	0.2020	0.2010	0.2003	3.0359	2.571
	$10K_{TNx}$	0.6964	0.7128	0.7126	0.0344	0.0004
	$10K_{QPx}$	0.4165	0.4146	0.4137	0.4742	0.2121
U_x (m s ⁻¹)	$x/D = 1$	0.4660	0.4828	0.4939	8.4981	5.4981
	$x/D = 2$	0.7226	0.7461	0.7449	0.1978	0.0095
	$x/D = 3$	0.9913	0.8860	0.9060	3.4658	0.6415
	$x/D = 4$	0.9829	0.9668	0.9633	0.5708	0.1231
	$x/D = 5$	1.0431	0.9921	1.0116	3.9693	1.4861
	$x/D = 6$	0.9309	0.9693	0.9946	4.3695	1.8611
	$x/D = 7$	0.9548	0.9556	0.9875	0.1073	4.1434
	$x/D = 8$	0.9692	0.9322	0.9406	1.4421	0.3223
	$x/D = 9$	0.9086	0.9869	0.9949	1.1344	0.1155

Table 5. Grid convergence analysis for the DP case with $J = 0.4$ and $\alpha = 0^\circ$ based on the thrust and torque coefficients and time-averaged, x -direction velocity U_x along the axis centreline using GCI.

are similar to the fine mesh results, and thus, the wake prediction based on the fine mesh is considered reliable.

A.2. Modal decomposition theory

Proper orthogonal decomposition (POD) and dynamic mode decomposition (DMD) are the most useful modal analysis methods to identify flow patterns via dimensionality reduction decomposition (Rowley & Dawson 2017; Taira *et al.* 2017; Brunton *et al.* 2022). The basic elements of POD and DMD are briefly reviewed, and detailed theories are presented in the cited references.

A.2.1. POD

The objective of POD analysis is to determine the optimal basis functions (modes) that best represent the given data. Roots of the POD can be traced to the diagonalization technique, which is ultimately related to the singular value decomposition (SVD). Given a snapshot matrix with its temporal mean subtracted $\mathbf{X} = [\mathbf{x}(t_1), \mathbf{x}(t_2), \dots, \mathbf{x}(t_m)] \in \mathbb{R}^{n \times m}$ (m is the snapshot number with each snapshot vector $\mathbf{x}(t_j) \in \mathbb{R}^n$ being sampled at a constant time interval $\Delta t_s = t_{j+1} - t_j$, $j = 1, 2, \dots, m - 1$ and n is the discretized spatial mesh number of the snapshot data), the SVD-based POD is computed by

$$\mathbf{X} = \boldsymbol{\Psi} \boldsymbol{\Sigma} \mathbf{V}^T, \tag{A1}$$

where $\boldsymbol{\Psi} = [\boldsymbol{\psi}_1, \boldsymbol{\psi}_2, \dots, \boldsymbol{\psi}_m] \in \mathbb{R}^{n \times m}$ is the left singular (POD mode) matrix, $\boldsymbol{\Sigma} = \text{diag}(\sigma_1, \sigma_2, \dots, \sigma_m) \in \mathbb{R}^{m \times m}$ is the singular value matrix and $\mathbf{V} = [\mathbf{v}_1, \mathbf{v}_2, \dots, \mathbf{v}_m] \in \mathbb{R}^{m \times m}$ is the right singular matrix. The POD time coefficient matrix \mathbf{A}_{POD} is obtained by

$$\mathbf{A}_{POD} = \boldsymbol{\Psi}^T \mathbf{X} = \boldsymbol{\Sigma} \mathbf{V}^T, \tag{A2}$$

where $\mathbf{A}_{POD} = [\mathbf{a}_1(t), \mathbf{a}_2(t), \dots, \mathbf{a}_m(t)]^T \in \mathbb{R}^{m \times m}$. Each POD mode is ranked according to the spatial information it contains, namely, $\sigma_1 \geq \sigma_2 \geq \dots \geq \sigma_m \geq 0$. The relative energy of the i th POD mode and the cumulative energy of the first i modes are defined

as

$$E_i = \sigma_i^2 / \sum_{j=1}^m \sigma_j^2, \quad E_i^{cum} = \sum_{k=1}^i E_k. \quad (\text{A3a,b})$$

A.2.2. DMD

The DMD algorithm proposed by Schmid (2010) assumes a time-invariant linear operator $\mathbf{O} \in \mathbb{R}^{n \times n}$ between adjacent snapshots $\mathbf{X}' = \mathbf{O}\mathbf{X}$, where the mean flow is retained in the snapshot matrices $\mathbf{X} = [\mathbf{x}(t_0), \mathbf{x}(t_1), \dots, \mathbf{x}(t_{m-1})] \in \mathbb{R}^{n \times m}$ and $\mathbf{X}' = [\mathbf{x}(t_1), \mathbf{x}(t_2), \dots, \mathbf{x}(t_m)] \in \mathbb{R}^{n \times m}$. The operator \mathbf{O} is then defined by $\mathbf{O} = \mathbf{X}'\mathbf{X}^\dagger$, where \dagger denotes the Moore–Penrose pseudoinverse. Since the size of \mathbf{O} ($n \times n$) is generally too large, it is inefficient to compute \mathbf{O} . Instead, an algorithm similar to the exact DMD algorithm proposed by Tu *et al.* (2014) is given as follows.

- (i) Perform the SVD of \mathbf{X} to obtain m orthogonal bases (POD modes), which makes $\mathbf{X} = \mathbf{\Psi}\mathbf{\Sigma}\mathbf{V}^T$, similar to (A1).
- (ii) Project \mathbf{O} onto the POD subspace; then, a reduced matrix $\tilde{\mathbf{O}}$ is defined as $\tilde{\mathbf{O}} = \mathbf{\Psi}^T\mathbf{O}\mathbf{\Psi} = \mathbf{\Psi}^T\mathbf{X}'\mathbf{V}\mathbf{\Sigma}^{-1} \in \mathbb{R}^{m \times m}$. The eigenvalue decomposition of $\tilde{\mathbf{O}}$ is computed by

$$\tilde{\mathbf{O}}\mathbf{W} = \mathbf{W}\mathbf{\Lambda}, \quad (\text{A4})$$

where $\mathbf{W} = [w_1, w_2, \dots, w_m] \in \mathbb{C}^{m \times m}$ and $\mathbf{\Lambda} = \text{diag}(\lambda_1, \lambda_2, \dots, \lambda_m) \in \mathbb{C}^{m \times m}$ are the eigenvector matrix of $\tilde{\mathbf{O}}$ and eigenvalue matrix of $\tilde{\mathbf{O}}$, respectively. Each non-zero λ_i is a DMD eigenvalue, and the DMD mode matrix $\mathbf{\Phi} = [\phi_1, \phi_2, \dots, \phi_m] \in \mathbb{C}^{m \times m}$ is then given by

$$\mathbf{\Phi} = \mathbf{X}'\mathbf{V}\mathbf{\Sigma}^{-1}\mathbf{W}\mathbf{\Lambda}^{-1}. \quad (\text{A5})$$

The growth rate matrix $\mathbf{G} = \text{diag}(g_1, g_2, \dots, g_m) \in \mathbb{R}^{m \times m}$ and modal frequency matrix $\mathbf{F} = \text{diag}(f_1, f_2, \dots, f_m) \in \mathbb{R}^{m \times m}$ are defined based on $\mathbf{\Lambda}$ as

$$\mathbf{G} = \ln(\text{Re}(\mathbf{\Lambda})) / \Delta t_s, \quad (\text{A6})$$

$$\mathbf{F} = \ln(\text{Im}(\mathbf{\Lambda})) / (2\pi \Delta t_s). \quad (\text{A7})$$

- (iii) With the DMD modes and eigenvalues, it is possible to approximately reconstruct the flow field \mathbf{X} :

$$\mathbf{X} \approx \underbrace{[\phi_1, \phi_2, \dots, \phi_m]}_{\mathbf{\Phi}} \underbrace{\begin{bmatrix} s_1 & & & \\ & s_2 & & \\ & & \ddots & \\ & & & s_m \end{bmatrix}}_{\mathbf{S}} \underbrace{\begin{bmatrix} 1 & \lambda_1 & \dots & \lambda_1^{m-1} \\ 1 & \lambda_2 & \dots & \lambda_2^{m-1} \\ \vdots & \vdots & \ddots & \vdots \\ 1 & \lambda_m & \dots & \lambda_m^{m-1} \end{bmatrix}}_{\mathbf{V}_{and}}, \quad (\text{A8})$$

where $\mathbf{S} \in \mathbb{C}^{m \times m}$ is the DMD amplitude matrix and $\mathbf{V}_{and} \in \mathbb{C}^{m \times m}$ is the Vandermonde matrix. The procedure for obtaining \mathbf{S} is written as a residual minimization problem: minimize $s \| \mathbf{X} - \mathbf{\Phi}\mathbf{S}\mathbf{V}_{and} \|_F$, where $\| \cdot \|$ is the Frobenius norm. Based on the solution of \mathbf{S} , the DMD time coefficient matrix

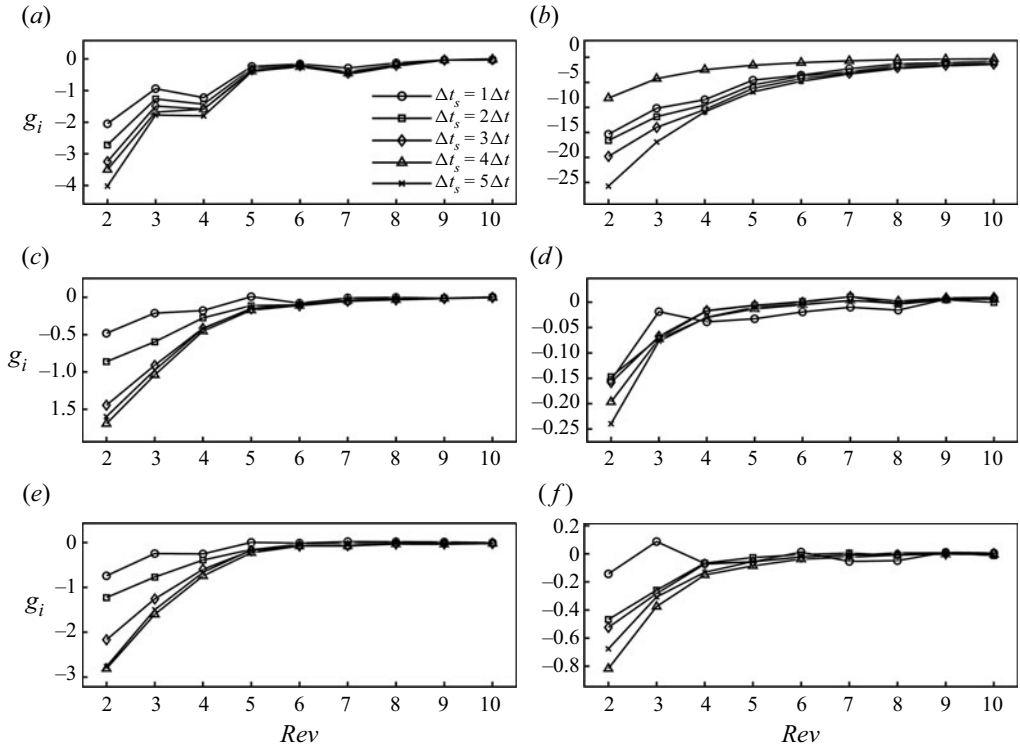


Figure 27. Variation in decay rate with sampling length and sampling time interval for $\kappa = 2, 4$ and 8 DMD modes for the (a, c and e) NP at $\alpha = 15^\circ$ and the (b, d and f) DP at $\alpha = 15^\circ$. (a) NP $\alpha = 15^\circ$, $\kappa = 2$ DMD mode; (b) DP $\alpha = 15^\circ$, $\kappa = 2$ DMD mode; (c) NP $\alpha = 15^\circ$, $\kappa = 4$ DMD mode; (d) DP $\alpha = 15^\circ$, $\kappa = 4$ DMD mode; (e) NP $\alpha = 15^\circ$, $\kappa = 8$ DMD mode and (f) DP $\alpha = 15^\circ$, $\kappa = 8$ DMD mode.

$\mathbf{A}_{DMD} = [\mathbf{a}_1(t), \mathbf{a}_2(t), \dots, \mathbf{a}_m(t)]^T \in \mathbb{C}^{m \times m}$ and the dynamic factor matrix $\mathbf{D} = \text{diag}(d_1, d_2, \dots, d_m) \in \mathbb{R}^{m \times m}$ proposed by Statnikov *et al.* (2017) are given by

$$\mathbf{A}_{DMD} = \mathbf{S}\mathbf{V}_{and}, \tag{A9}$$

$$\mathbf{D} = |\mathbf{S}| \times |\mathbf{A}|^m, \tag{A10}$$

where $|\cdot|$ returns the absolute value of each element in the matrix.

A.3. Modal convergence analysis

The modal convergence is determined by the sampling time interval Δt_s and sampling size of the dataset. The sample size is the overall length of the time window in the modal analysis, which is measured in revolutions (*Rev*). The converged dataset should ensure that the modal results no longer vary with the decreasing sampling time interval and the increasing sampling size. Thus, the modal convergence analysis focuses on the modal growth/decay rate in (A6), amplitude (A8), spatial morphology (A5) and temporal coefficients (A2) and (A9).

According to the Nyquist-Shannon criterion (Desoer & Wang 1979), the snapshot sampling frequency f_{samp} should be at least two times the shaft frequency f_{shaft} to capture flow features in the range of the shaft frequency, i.e. $f_{samp} = 1/\Delta t_s \geq 2f_{shaft} = 35.3$ Hz. Based on the numerical output interval of $\Delta t = 4.725 \times 10^{-4}$ s (§ 2.2), a series of time

Effects of a nozzle on the propeller wake

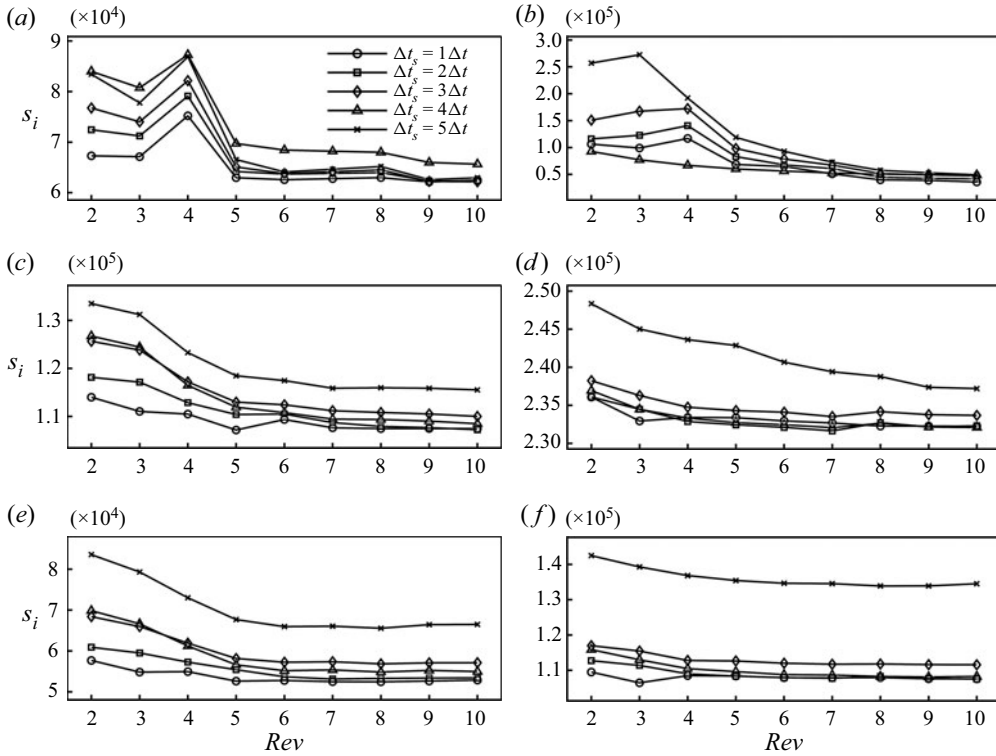


Figure 28. Variation in amplitude with sampling length and sampling time interval for $\kappa = 2, 4$ and 8 DMD modes for the (a, c and e) NP at $\alpha = 15^\circ$ and the (b, d and f) DP at $\alpha = 15^\circ$. (a) NP $\alpha = 15^\circ$, $\kappa = 2$ DMD mode; (b) DP $\alpha = 15^\circ$, $\kappa = 2$ DMD mode; (c) NP $\alpha = 15^\circ$, $\kappa = 4$ DMD mode; (d) DP $\alpha = 15^\circ$, $\kappa = 4$ DMD mode; (e) NP $\alpha = 15^\circ$, $\kappa = 8$ DMD mode and (f) DP $\alpha = 15^\circ$, $\kappa = 8$ DMD mode.

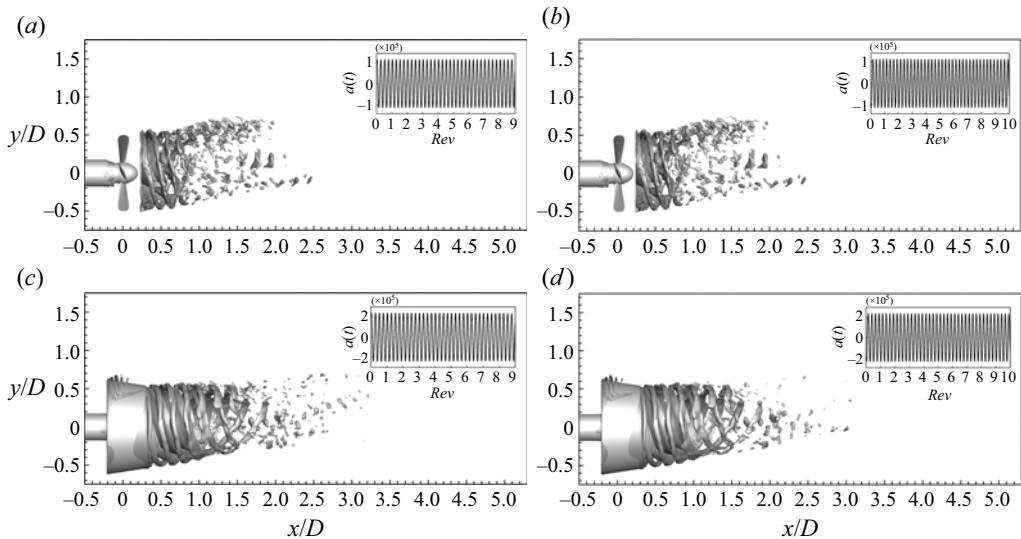


Figure 29. Comparison of spatial morphology of the $\kappa = 4$ DMD modes obtained based on the datasets covering nine and ten revolutions with the time interval $\Delta t_s = 1 \Delta t$ for the (a,b) NP at $\alpha = 15^\circ$ and the (c,d) DP at $\alpha = 15^\circ$. (a) NP $\alpha = 15^\circ$, $Rev = 9$; (b) NP $\alpha = 15^\circ$, $Rev = 10$; (c) DP $\alpha = 15^\circ$, $Rev = 9$ and (d) DP $\alpha = 15^\circ$, $Rev = 10$.

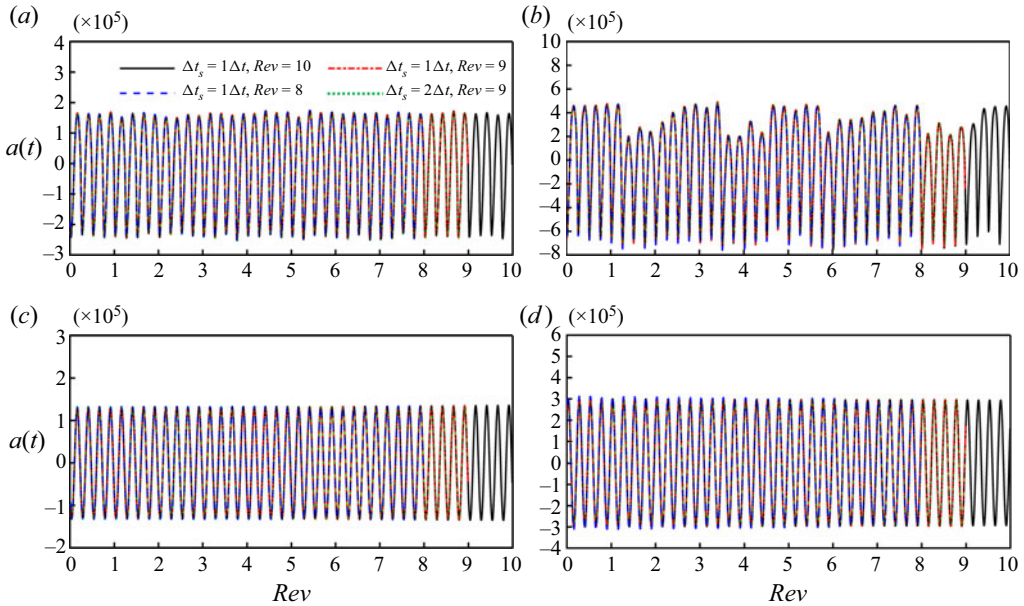


Figure 30. Comparison of time coefficient between the (a,b) first POD mode and the (c,d) real part of $\kappa = 4$ DMD mode for the NP and DP at $\alpha = 60^\circ$ obtained based on different datasets. (a) NP $\alpha = 60^\circ$, first POD mode; (b) DP $\alpha = 60^\circ$, first POD mode; (c) NP $\alpha = 60^\circ$, $\kappa = 4$ POD mode and (d) DP $\alpha = 60^\circ$, $\kappa = 4$ POD mode.

intervals $\Delta t_s = [1, 2, 3, 4, 5]\Delta t$ is set to investigate the effect of the time interval on the modal convergence, and these time intervals can resolve the modes in the frequency range of $\kappa \leq 60, 30, 20, 15$ and 12 , respectively. Moreover, DMD is not sensitive to whether the dataset covers an integer number of periods (Chen *et al.* 2012), but POD might generate spurious modes when the dataset does not cover integral periods. Therefore, the modal convergence study is conducted on the datasets covering 2–10 revolutions.

In figure 15, the $\kappa = 2, 4$ and 8 DMD modes are important for the NP and DP wakes, and the decay rate and amplitude of these representative modes serve as measures for modal convergence, as shown in figures 27 and 28. For the NP and DP at $\alpha = 15^\circ$, the decay rate and amplitude stop changing when the sampling size reaches nine revolutions, and the differences between the results from $\Delta t_s = 1\Delta t$ and $2\Delta t$ are negligibly small at nine revolutions.

Figure 29 shows the spatial morphologies of the $\kappa = 4$ DMD modes obtained by the datasets covering nine and ten revolutions with $\Delta t_s = 1\Delta t$ for the NP and DP at $\alpha = 15^\circ$. The results show negligible differences in morphologies between nine and ten revolutions for both the NP and DP at $\alpha = 15^\circ$. Figure 30 further compares the time coefficients of the first POD modes and the real part of the $\kappa = 4$ DMD modes obtained by four different datasets ($\Delta t_s = 1\Delta t$, ten revolutions; $\Delta t_s = 1\Delta t$, nine revolutions; $\Delta t_s = 1\Delta t$, eight revolutions; and $\Delta t_s = 2\Delta t$, nine revolutions) for the NP and DP at $\alpha = 60^\circ$. Even for the severely destabilized cases (figures 17–19), the dataset with $\Delta t_s = 1\Delta t$ and nine revolutions can identify the fluctuations in the time coefficients, and its results match those obtained by the other three datasets. Based on the analysis above, for each case, a dataset with a time interval of $\Delta t_s = 1\Delta t$ and a sampling size of nine revolutions is eventually chosen for modal analysis.

Effects of a nozzle on the propeller wake

REFERENCES

- AARON, T., SCHMIDT, O.T. & COLONIUS, T. 2018 Spectral proper orthogonal decomposition and its relationship to dynamic mode decomposition and resolvent analysis. *J. Fluid Mech.* **847**, 821–867.
- AHMED, S., CROAKER, P. & DOOLAN, C.J. 2020 On the instability mechanisms of ship propeller wakes. *Ocean Engng* **213**, 107609.
- ALLEN, J.J. & AUVITY, B. 2002 Interaction of a vortex ring with a piston vortex. *J. Fluid Mech.* **465**, 353–378.
- ASHTON, R., VIOLA, F., CAMARRI, S., GALLAIRE, F. & IUNGO, G.V. 2016 Hub vortex instability within wind turbine wakes: effects of wind turbulence, loading conditions, and blade aerodynamics. *Phys. Rev. Fluids* **1**, 1–18.
- BASTANKHAH, M. & PORTÉ-AGEL, F. 2016 Experimental and theoretical study of wind turbine wakes in yawed conditions. *J. Fluid Mech.* **806**, 506–541.
- BASTANKHAH, M. & PORTÉ-AGEL, F. 2017 Wind tunnel study of the wind turbine interaction with a boundary-layer flow: upwind region, turbine performance, and wake region. *Phys. Fluids* **29**, 065105.
- BORG, M.G., XIAO, Q., ALLSOP, S., INCECIK, A. & PEYRARD, C. 2020 A numerical performance analysis of a ducted, high-solidity tidal turbine in yawed flow conditions. *Renew. Energy* **193**, 179–194.
- BOSSUYT, J., SCOTT, R., ALI, N. & CAL, R.B. 2021 Quantification of wake shape modulation and deflection for tilt and yaw misaligned wind turbines. *J. Fluid Mech.* **917**, A3.
- BRUNTON, S.L., BUDIŠIĆ, M., KAISER, E. & KUTZ, J.N. 2022 Modern Koopman theory for dynamical systems. *SIAM Rev.* **64**, 229–340.
- CELIK, I., GHIA, U., ROACHE, P.J., FREITAS, C., COLOMAN, H. & RAAD, P. 2008 Procedure of estimation and reporting of uncertainty due to discretization in CFD applications. *Trans. ASME J. Fluids Engng* **130**, 078001.
- CHEN, K.K., TU, J.H. & ROWLEY, C.W. 2012 Variants of dynamic mode decomposition: boundary condition, Koopman, and fourier analyses. *J. Nonlinear Sci.* **22**, 887–915.
- COZIUN, J. & HALLMANN, R. 2012 The wake flow behind azimuthing thrusters: measurements in open water, under a plate and under a barge. In *Proceedings of the ASME 2012 31st International Conference on Ocean, Offshore and Arctic Engineering, Rio de Janeiro, Brazil*. ASME.
- COZIUN, J.L., HALLMANN, R. & KOOP, A.H. 2010 Analysis of the velocities in the wake of an azimuthing thruster, using PIV measurements and CFD calculations. In *Proceedings of Dynamic Positioning Conference, Houston, Texas, USA*.
- DE CILLIS, G., CHERUBINI, S., SEMERARO, O., LEONARDI, S. & DE PALMA, P. 2022a The influence of incoming turbulence on the dynamic modes of an NREL-5MW wind turbine wake. *Renew. Energy* **183**, 601–616.
- DE CILLIS, G., CHERUBINI, S., SEMERARO, O., LEONARDI, S. & DE PALMA, P. 2022b Stability and optimal forcing analysis of a wind turbine wake: comparison with POD. *Renew. Energy* **181**, 765–785.
- DEBNATH, M., SANTONI, C., LEONARDI, S. & IUNGO, G.V. 2017 Towards reduced order modelling for predicting the dynamics of coherent vorticity structures within wind turbine wakes. *Phil. Trans. R. Soc. A* **375**, 20160108.
- DESOER, C. & WANG, Y.T. 1979 On the generalized nyquist stability criterion. In *Proceedings of the 18th IEEE Conference on Decision and Control including the Symposium on Adaptive Processes, Fort Lauderdale, USA*. IEEE.
- DI FELICE, F., DI FLORIO, D., FELLI, M. & ROMANO, G. 2004 Experimental Investigation of the propeller wake at different loading conditions by particle image velocimetry. *J. Ship Res.* **48**, 168–190.
- DI MASCIO, A., MUSCARI, R. & DUBBIOSO, G. 2014 On the wake dynamics of a propeller operating in drift. *J. Fluid Mech.* **754**, 263–307.
- DUBBIOSO, G., MUSCARI, R. & DI MASCIO, A. 2013 Analysis of the performances of a marine propeller operating in oblique flow. *Comput. Fluids* **75**, 86–102.
- DUBBIOSO, G., MUSCARI, R. & DI MASCIO, A. 2014 Analysis of a marine propeller operating in oblique flow. Part 2: very high incidence angles. *Comput. Fluids* **92**, 56–81.
- FARRELL, P.E. & MADDISON, J.R. 2011 Conservative interpolation between volume meshes by local Galerkin projection. *Comput. Meth. Appl. Mech. Engng* **200**, 89–100.
- FELLI, M., CAMUSSI, R. & DI FELICE, F. 2011 Mechanisms of evolution of the propeller wake in the transition and far fields. *J. Fluid Mech.* **682**, 5–53.
- FELLI, M. & DI FELICE, F. 2005 Propeller wake analysis in nonuniform inflow by LDV phase sampling techniques. *J. Mar. Sci. Technol.* **10**, 159–172.
- FELLI, M., DI FELICE, F. & GUJ, G. 2006 Analysis of the propeller wake evolution by pressure and velocity phase measurements. *Exp. Fluids* **41**, 441–451.
- FELLI, M. & FALCHI, M. 2018 Propeller wake evolution mechanisms in oblique flow conditions. *J. Fluid Mech.* **845**, 520–559.

- FELLI, M., FALCHI, M. & DUBBIOSO, G. 2015 Hydrodynamic and Hydroacoustic analysis of a marine propeller wake by TOMO-PIV. In *Proceedings of the Fourth International Symposium on Marine Propulsors (SMP'15)*, Austin, Texas, USA. SMP.
- FOTI, D., YANG, X.L., CAMPAGNOLO, F., MANIACI, D. & SOTIROPOULOS, F. 2018a Wake meandering of a model wind turbine operating in two different regimes. *Phys. Rev. Fluids* **3**, 054607.
- FOTI, D., YANG, X.L., GUALA, M. & SOTIROPOULOS, F. 2016 Wake meandering statistics of a model wind turbine: insights gained by large eddy simulations. *Phys. Rev. Fluids* **1**, 044407.
- FOTI, D., YANG, X.L., SHEN, L. & SOTIROPOULOS, F. 2019 Effect of wind turbine nacelle on turbine wake dynamics in large wind farms. *J. Fluid Mech.* **869**, 1–26.
- FOTI, D., YANG, X.L. & SOTIROPOULOS, F. 2018b Similarity of wake meandering for different wind turbine designs for different scales. *J. Fluid Mech.* **842**, 5–25.
- GONG, J., DING, J.M. & WANG, L.Z. 2021 Propeller–duct interaction on the wake dynamics of a ducted propeller. *Phys. Fluids* **33**, 074102.
- GONG, J., GUO, C.Y., ZHAO, D.G., WU, T.C. & SONG, K.W. 2018 A comparative DES study of wake vortex evolution for ducted and non-ducted propellers. *Ocean Engng* **160**, 78–93.
- GUPTA, V. & WAN, M.P. 2019 Low-order modelling of wake meandering behind turbines. *J. Fluid Mech.* **877**, 534–560.
- HAMILTON, N., TUTKUN, M. & CAL, R.B. 2015 Wind turbine boundary layer arrays for Cartesian and staggered configurations: part II, low-dimensional representations via the proper orthogonal decomposition. *Wind Energy* **18**, 297–315.
- HOWARD, K.B., SINGH, A., SOTIROPOULOS, F. & GUALA, M. 2015 On the statistics of wind turbine wake meandering: an experimental investigation. *Phys. Fluids* **27**, 075103.
- HUANG, Q.G., QIN, D.H. & PAN, G. 2022 Numerical simulation of the wake dynamics of the pumpjet propulsor in oblique inflow. *Phys. Fluids* **34**, 065103.
- IUNGO, G.V., SANTONI-ORTIZ, C., ABKAR, M., PORTÉ-AGEL, F., ROTEA, M.A. & LEONARDI, S. 2015 Data-driven reduced order model for prediction of wind turbine wakes. *J. Phys.: Conf. Ser.* **625**, 012009.
- IUNGO, G.V., VIOLA, F., CAMARRI, S., PORTÉ-AGEL, F. & GALLAIRE, F. 2013 Linear stability analysis of wind turbine wakes performed on wind tunnel measurements. *J. Fluid Mech.* **737**, 499–526.
- JOUKOWSKY, N.E. 1912 Vortex theory of screw propeller. *Tr. Otd. Fiz. Nauk O-va Lyubit. Estestvoznan* **16**, 1–31.
- JOVANOVIĆ, M.R., SCHMID, P.J. & NICHOLS, J.W. 2014 Sparsity-promoting dynamic mode decomposition. *Phys. Fluids* **26**, 1–22.
- KANG, S., YANG, X.L. & SOTIROPOULOS, F. 2014 On the onset of wake meandering for an axial flow turbine in a turbulent open channel flow. *J. Fluid Mech.* **744**, 376–403.
- KOOP, A., COZIJJN, H., SCHRIJVERS, P. & VAZ, G. 2017 Determining thruster-hull interaction for a drill-ship using CFD. In *Proceedings of the ASME 2017 36th International Conference on Ocean, Offshore and Arctic Engineering, Trondheim, Norway*. ASME.
- KUMAR, P. & MAHESH, K. 2015 Analysis of marine propulsor in crashback using large eddy simulation. In *Proceedings of the Fourth International Symposium on Marine Propulsors (SMP'15)*. Austin, Texas, USA. SMP.
- KUMAR, P. & MAHESH, K. 2017 Large eddy simulation of propeller wake instabilities. *J. Fluid Mech.* **814**, 361–396.
- LE, T.B., BORAZJANI, I., KANG, S. & SOTIROPOULOS, F. 2011 On the structure of vortex rings from inclined nozzles. *J. Fluid Mech.* **686**, 451–483.
- LI, H., HUANG, Q.G., PAN, G., DONG, X.G. & LI, F.Z. 2022 An investigation on the flow and vortical structure of a pre-swirl stator pump-jet propulsor in drift. *Ocean Engng* **250**, 111061.
- LI, Z.B. & YANG, X.L. 2021 Large-eddy simulation on the similarity between wakes of wind turbines with different yaw angles. *J. Fluid Mech.* **921**, A11.
- LUMLEY, J.L. 1970 *Stochastic Tools in Turbulence*. Academic Press.
- MACIEL, P., KOOP, A. & VAZ, G. 2013 Modelling thruster-hull interaction with CFD. In *Proceedings of the ASME 2013 32nd International Conference on Ocean, Offshore and Arctic Engineering, Nantes, France*. ASME.
- MAGIONESI, F., DUBBIOSO, G., MUSCARI, R. & DI MASCIIO, A. 2018 Modal analysis of the wake past a marine propeller. *J. Fluid Mech.* **855**, 469–502.
- MAO, X. & SØRENSEN, J.N. 2018 Far-wake meandering induced by atmospheric eddies in flow past a wind turbine. *J. Fluid Mech.* **846**, 190–209.
- MICALLEF, D. & SANT, T. 2016 *A Review of Wind Turbine Yaw Aerodynamics*. IntechOpen.
- MUSCARI, R., DI MASCIIO, A. & VERZICCO, R. 2013 Modeling of vortex dynamics in the wake of a marine propeller. *Comput. Fluids* **73**, 65–79.

- MUSCARI, R., DUBBIOSO, G. & DI MASCIIO, A. 2017 Analysis of the flow field around a rudder in the wake of a simplified marine propeller. *J. Fluid Mech.* **814**, 547–569.
- NEMES, A., SHERRY, M., JACONO, D.L., BLACKBURN, H.M. & SHERIDAN, J. 2014 Evolution and breakdown of helical vortex wakes behind a wind turbine. *J. Phys.: Conf. Ser.* **555**, 012077.
- NOACK, B.R., STANKIEWICZ, W., MORZYŃSKI, M. & SCHMID, P.J. 2016 Recursive dynamic mode decomposition of transient and post-transient wake flows. *J. Fluid Mech.* **809**, 843–872.
- OKULOV, V. 2004 On the stability of multiple helical vortices. *J. Fluid Mech.* **521**, 319–342.
- OKULOV, V. & SØRENSEN, J. 2007 Stability of helical tip vortices in rotor far wake. *J. Fluid Mech.* **576**, 1–25.
- PAIK, B.G., KYUNG, Y.K., JUNG, Y.L. & SANG, J.L. 2010 Analysis of unstable vortical structure in a propeller wake affected by a simulated hull wake. *Exp. Fluids* **48**, 1121–1133.
- POSA, A. & BROGLIA, R. 2021 Flow over a hydrofoil at incidence immersed within the wake of a propeller. *Phys. Fluids* **33**, 125108.
- POSA, A., BROGLIA, R. & BALARAS, E. 2020 The wake structure of a propeller operating upstream of a hydrofoil. *J. Fluid Mech.* **904**, A12.
- POSA, A., BROGLIA, R. & BALARAS, E. 2022 Recovery in the wake of in-line axial-flow rotors. *Phys. Fluids* **34**, 045104.
- POSA, A., BROGLIA, R., FELLI, M., FALCHI, M. & BALARAS, E. 2019 Characterization of the wake of a submarine propeller via large-Eddy simulation. *Comput. Fluids* **184**, 138–152.
- QATramez, A.E. & Foti, D. 2021 Reduced-order model predictions of wind turbines via mode decomposition and sparse sampling. In *AIAA Scitech 2021 Forum*. American Institute of Aeronautics and Astronautics.
- QIN, D.H., HUANG, Q.G., PAN, G., HAN, P., LUO, Y. & DONG, X.G. 2021 Numerical simulation of vortex instabilities in the wake of a preswirl pumpjet propulsor. *Phys. Fluids* **33**, 055119.
- QIU, C.C., PAN, G., HUANG, Q.G. & SHI, Y. 2020 Numerical analysis of unsteady hydrodynamic performance of pump-jet propulsor in oblique flow. *Int. J. Nav. Arch. Ocean Engng* **12**, 102–115.
- RICCA, R. 1994 Effect of torsion on the motion of a helical vortex filament. *J. Fluid Mech.* **273**, 241–259.
- ROWLEY, C.W. & DAWSON, S. 2017 Model reduction for flow analysis and control. *Annu. Rev. Fluid Mech.* **49**, 387–417.
- ROWLEY, C.W., MEZIĆ, I., BAGHERI, S., SCHLATTER, P. & HENNINGSON, D.S. 2009 Spectral analysis of nonlinear flows. *J. Fluid Mech.* **641**, 115–127.
- RUMSEY, C.L. 2007 Apparent transition behavior of widely-used turbulence models. *Intl J. Heat Fluid Flow* **28**, 1460–1471.
- SARMAST, S., DADFAR, R., MIKKELSEN, R.F., SCHLATTER, P., IVANELL, S., SØRENSEN, J.N. & HENNINGSON, D.S. 2014 Mutual inductance instability of the tip vortices behind a wind turbine. *J. Fluid Mech.* **755**, 705–731.
- SCHMID, P.J. 2010 Dynamic mode decomposition of numerical and experimental data. *J. Fluid Mech.* **656**, 5–28.
- SCHMID, P.J., VIOLATO, D. & SCARANO, F. 2012 Decomposition of time-resolved tomographic PIV. *Exp. Fluids* **52**, 1567–1579.
- SHI, H.D., WANG, T.Y., ZHAO, M. & ZHANG, Q. 2022 Modal analysis of non-ducted and ducted propeller wake under axis flow. *Phys. Fluids* **34**, 055128.
- SHUR, M.L., SPALART, P.R., STRELETS, M.K. & TRAVIN, A.K. 1999 Detached-eddy simulation of an airfoil at high angle of attack. In *4th International Symposium on Engineering Turbulence Modelling and Measurements* (ed. W. Rodi & D. Laurence), pp. 669–678. Elsevier Science Ltd.
- SIROVICH, L. 1987 Turbulence and the dynamics of coherent structures. I-coherent structures. II-symmetries and transformations. III-dynamics and scaling. *Q. Appl. Maths* **45**, 561–571.
- SPALART, P.R. & ALLMARAS, S.R. 1992 A one-equation turbulence model for aerodynamic flows. In *30th Aerospace Sciences Meeting and Exhibit*. American Institute of Aeronautics and Astronautics.
- SPALART, P.R., DECK, S., SHUR, M.L., SQUIRES, K.D., STRELETS, M.K. & TRAVIN, A.K. 2006 A new version of detached-eddy simulation, resistant to ambiguous grid densities. *Theor. Comput. Fluid Dyn.* **20**, 181–195.
- SPALART, P.R., SHUR, M.L., STRELETS, M.K. & TRAVIN, A.K. 2012 Sensitivity of landing-gear noise predictions by large-eddy simulation to numerics and resolution. In *50th AIAA Aerospace Sciences Meeting including the New Horizons Forum and Aerospace Exposition*. American Institute of Aeronautics and Astronautics.
- STATNIKOV, V., MEINKE, M. & SCHRÖDER, W. 2017 Reduced-order analysis of buffet flow of space launchers. *J. Fluid Mech.* **815**, 1–25.

- STEINFURTH, B. & WEISS, J. 2020 Vortex rings produced by non-parallel planar starting jets. *J. Fluid Mech.* **903**, A16.
- SUN, C., TIAN, T., ZHU, X.C., HUA, O.Y. & DU, Z.H. 2021 Investigation of the near wake of a horizontal-axis wind turbine model by dynamic mode decomposition. *Energy* **227**, 120418.
- TAIRA, K., BRUNTON, S.L., DAWSON, S.T.M., ROWLEY, C.W., COLONIUS, T., MCKEON, B.J., SCHMIDT, O.T., GORDEYEV, S., THEOFILIS, V. & UKEILEY, L.S. 2017 Modal analysis of fluid flows: an overview. *AIAA J.* **55**, 1–29.
- TRAVIN, A., SHUR, M., STRELETS, M. & SPALART, P.R. 2002 Physical and numerical upgrades in the detached-eddy simulation of complex turbulent flows. In *Advances in LES of Complex Flows* (ed. R. Friedrich & W. Rodi), pp. 239–254. Springer.
- TU, J.H., ROWLEY, C.W., LUCHTENBURG, D.M., BRUNTON, S.L. & KUTZ, J.N. 2014 On dynamic mode decomposition: theory and applications. *J. Comput. Dyn.* **1**, 391–421.
- VERMA, A., JANG, H. & MAHESH, K. 2012 The effect of an upstream hull on a propeller in reverse rotation. *J. Fluid Mech.* **704**, 61–88.
- VIOLA, F., IUNGO, G.V., CAMARRI, S., PORTÉ-AGEL, F. & GALLAIRE, F. 2014 Prediction of the hub vortex instability in a wind turbine wake: stability analysis with eddy-viscosity models calibrated on wind tunnel data. *J. Fluid Mech.* **750**, R1.
- VIOLA, F., IUNGO, G.V., CAMARRI, S., PORTÉ-AGEL, F. & GALLAIRE, F. 2015 Instability of wind turbine wakes immersed in the atmospheric boundary layer. *J. Phys.: Conf. Ser.* **625**, 012034.
- VIVIANI, M., BONVINO, C., MAURO, S., CERRUTI, M., GUADALUPI, D. & MENNA, A. 2007 Analysis of asymmetrical shaft power increase during tight maneuvers. In *9th International Conference on Fast Sea Transportation (FAST 2007)*, Shanghai, China. GICAN.
- WANG, L.Z., GUO, C.Y., XU, P. & SU, Y.M. 2019 Analysis of the wake dynamics of a propeller operating before a rudder. *Ocean Engng* **188**, 106250.
- WANG, L.Z., LIU, X.Y. & WU, T.C. 2022 Modal analysis of the propeller wake under the heavy loading condition. *Phys. Fluids* **34**, 055107.
- WANG, L.Z., WU, T.C., GONG, J. & YANG, Y.R. 2021a Numerical analysis of the wake dynamics of a propeller. *Phys. Fluids* **33**, 095120.
- WANG, L.Z., WU, T.C., GONG, J. & YANG, Y.R. 2021b Numerical simulation of the wake instabilities of a propeller. *Phys. Fluids* **33**, 125125.
- WIDNALL, S.E. 1972 The stability of a helical vortex filament. *J. Fluid Mech.* **54**, 641–663.
- WU, J.Z., MA, H.Y. & ZHOU, M.D. 2006 *Vorticity and Vortex Dynamics*. Springer.
- YANG, X.L. & SOTIROPOULOS, F. 2019 A review on the meandering of wind turbine wakes. *Energies* **12**, 1–20.
- ZHANG, Q. & JAIMAN, R.K. 2019 Numerical analysis on the wake dynamics of a ducted propeller. *Ocean Engng* **171**, 202–224.
- ZHANG, Q., MA, P.F. & LIU, J. 2018 Investigation on the performance of a ducted propeller in oblique flow. *Trans. ASME J. Offshore Mech. Arctic Engng* **142**, 011801.
- ZHANG, W.P., MARKFORT, C.D. & PORTÉ-AGEL, F. 2012 Near-wake flow structure downwind of a wind turbine in a turbulent boundary layer. *Exp. Fluids* **52**, 1219–1235.
- ZHANG, W.P., NING, X.S., LI, F.G., GUO, H. & SUN, S.L. 2021 Vibrations of simplified rudder induced by propeller wake. *Phys. Fluids* **33**, 083618.
- ZONG, H. & PORTÉ-AGEL, F. 2020 A point vortex transportation model for yawed wind turbine wakes. *J. Fluid Mech.* **890**, A8.